bioRxiv preprint doi: https://doi.org/10.1101/2020.12.04.411645; this version posted December 4, 2020. The copyright holder for this preprint (which was not certified by peer review) is the author/funder, who has granted bioRxiv a license to display the preprint in perpetuity. It is made available under aCC-BY-NC-ND 4.0 International license.

CYRI-A regulates macropinocytic cup maturation and mediates integrin uptake, limiting invasive migration

Anh Hoang Le[1], Tamas Yelland[1], Nikki R. Paul[1], Loic Fort[1,2], Savvas Nikolaou[1], Shehab Ismail[1], Laura M. Machesky[%,1,3]

[1] Cancer Research UK Beatson Institute, Bearden, Glasgow, UK.

[2] Department of Cell and Developmental Biology, Medical Research Building III, Vanderbilt University, Nashville, TN, USA.

[3] Institute of Cancer Sciences, University of Glasgow, UK.

[%] Author to whom correspondence should be addressed

l.machesky@beatson.gla.ac.uk

bioRxiv preprint doi: https://doi.org/10.1101/2020.12.04.411645; this version posted December 4, 2020. The copyright holder for this preprint (which was not certified by peer review) is the author/funder, who has granted bioRxiv a license to display the preprint in perpetuity. It is made available under aCC-BY-NC-ND 4.0 International license.

Abstract

The Scar/WAVE complex is the major driver of actin nucleation at the plasma membrane, resulting in lamellipodia and membrane ruffles. While lamellipodia aid migration, membrane ruffles can generate macropinosomes - cup-like structures - important for nutrient uptake and regulation of cell surface receptor levels. How macropinosomes are formed and the role of the actin machinery in their formation and resolution is still not well understood. Mammalian CYRI-B is a recently described negative regulator of the Scar/WAVE complex by RAC1 sequestration, but its other paralogue, CYRI-A has not been characterised. Here we implicate CYRI-A as a key regulator of macropinocytosis maturation and integrin internalisation from the cell surface. We find that CYRI-A is recruited to nascent macropinosomes in a transient but distinct burst, downstream of PIP3-mediated RAC1 activation to regulate actin polymerisation. CYRI-A precedes RAB5A recruitment to engulfed macropinocytic cups and departs as RAB5A is recruited, consistent with a role for CYRI-A as a local suppressor of actin dynamics, enabling the resolution of the macropinocytic cup. The suppression of integrin $\alpha5\beta1$ uptake caused by the co-depletion of CYRI-A and B in Ewing's sarcoma cells, leads to an enhancement of surface integrin levels and enhanced invasion and anchorage-independent growth in 3D. Thus CYRI-A is a dynamic regulator of integrin uptake via macropinocytosis, functioning together with CYRI-B to regulate integrin homeostasis on the cell surface.

Introduction

The actin cytoskeleton is a multifaceted network involved in many essential cellular processes including but not limited to cell migration and endocytosis. The small GTPase RAC1 acts as a regulatory switch at the heart of this network. By activating the Scar/WAVE complex, RAC1 indirectly triggers Arp2/3 complex activation and thus branched actin polymerisation.

RAC1-induced actin polymerisation is important in many endocytic processes (Bloomfield and Kay, 2016; Egami et al., 2014; Hinze, 2018; Ferreira and Boucrot, 2018; Mooren et al., 2012). The branched actin network is thought to induce membrane ruffling, a pre-requisite for macropinocytosis, or counteract the membrane tension exerted by the cytoplasmic hydrostatic force to drive membrane curvature and invagination (Carlsson, 2018). However, following RAC1 activation,

bioRxiv preprint doi: https://doi.org/10.1101/2020.12.04.411645; this version posted December 4, 2020. The copyright holder for this preprint (which was not certified by peer review) is the author/funder, who has granted bioRxiv a license to display the preprint in perpetuity. It is made available under aCC-BY-NC-ND 4.0 International license.

RAC1 inactivation is also essential for the completion of macropinocytosis (Fujii et al., 2013; Yoshida et al., 2009). Constitutively activating RAC1 by photoactivation led to unresolved membrane invagination until photoactivation was turned off (Fujii et al., 2013). The related process phagocytosis requires several GAPs in the deactivation of RAC1 but only for particles that are larger than 8μm (Schlam et al., 2015). However, whether these GAPs are involved in macropinocytosis remain unknown. Evidence suggests that a balanced spatial and temporal regulation of RAC1 and its downstream cytoskeletal targets at the site of endocytosis is essential.

Integrins are type-I transmembrane proteins important in cell adhesion and migration. Many of the integrin subunits and complexes along with their endocytic trafficking have been implicated in cancer cell invasion and metastasis (Caswell et al., 2009; Cooper and Giancotti, 2019). In breast cancer, increased surface expression of integrin α5 increases the cell contraction force and invasion (Mierke et al., 2011). In ovarian cancer, integrin α5β1 can be transported towards the invasive front by the WASH complex to increase invasion in 3D (Zech et al., 2011). Among the trafficking routes such as clathrin- or caveolin-1 dependent endocytosis (Shi and Sottile, 2008), bulk internalisation pathways like macropinocytosis and the CLIC-GEEG pathway have been shown to be involved in integrin trafficking and can affect the migration and invasion behaviour of cells (Gu et al., 2011; Moreno-Layseca et al., 2020).

Recently, we identified CYRI proteins as negative regulators of the regulation of the Scar/WAVE complex by RAC1 (Fort et al., 2018). Apart from cell migration, actin polymerisation by the Scar/WAVE complex has also been implicated in uptake of cellular pathogens and nutrients by macropinocytosis and phagocytosis (Humphreys et al., 2016; Veltman et al., 2016; Yuki et al., 2019). Indeed, CYRI-B has been implicated in reducing *Salmonella* infection (Yuki et al., 2019), regulating T-cell activation (Shang et al., 2018) and potentially acting as a tumour suppressor (Chattaragada et al., 2018). Mammalian cells possess two paralogs of the CYRI protein family named CYRI-A and CYRI-B, which are encoded by the *FAM49A* and *FAM49B* gene, respectively. Nothing is currently known about the cellular function of CYRI-A and its relationship with CYRI-B. By using a combination of biochemical analysis and live-cell imaging, we explore the membrane kinetics and the subcellular localisation of CYRIs, with a strong focus on CYRI-A, for the first time and implicate

bioRxiv preprint doi: https://doi.org/10.1101/2020.12.04.411645; this version posted December 4, 2020. The copyright holder for this preprint (which was not certified by peer review) is the author/funder, who has granted bioRxiv a license to display the preprint in perpetuity. It is made available under aCC-BY-NC-ND 4.0 International license.

their roles as novel regulators of macropinocytosis. We then connect the function of both CYRI-A and B to the trafficking of integrin α5β1 and their effects on cell migration, cell spreading and cancer cell invasion. We propose CYRI proteins as suppressors of the RAC1-actin signalling axis specifically at the macropinocytic cups to ensure efficient completion and maturation of macropinosomes.

Results

CYRI-A suppresses lamellipodial spreading and binds active RAC1

While CYRI-B has been characterised as a RAC1-binding protein that restricts lamellipodia, the role of CYRI-A is unknown. Deletion of CYRI-B promotes a broad lamellipodia phenotype with the enrichment of the Scar/WAVE complex at the leading edge (Fort et al., 2018; Yuki et al., 2019). To query whether CYRI-A expression could rescue the cell spreading phenotype caused by depletion of CYRI-B, we expressed either a FLAG-tagged GFP (control) or CYRI-A-FLAG (Fig. 1 A) in control or CYRI-B knockout (KO) COS-7 cells and measured the change in cell area and the average intensity of the Arp2/3 complex around the cell periphery. CYRI-B KO cells showed enhanced lamellipodia spreading as expected (Fort et al., 2018) (Fig. 1 A), which was rescued by re-expression of CYRI-A both in the spreading area (Fig. 1 B) and the Arp2/3 signal (Fig. 1 C). Western blot shows comparable levels of overexpression of CYRI-A-FLAG between cell lines (Fig. 1 D). Expression of untagged CYRI-A using a bi-cistronic system also rescued the spread area and Arp2/3 recruitment (Fig. S1 A). This suggests that the expression of CYRI-A can suppress the exaggerated spreading and increase in lamellipodia induced by loss of CYRI-B, suggesting similar functions of these two proteins in controlling lamellipodia.

We next queried whether CYRI-A could interact with active RAC1. Using the I-TASSER protein prediction tool along with the recently solved crystal structure of CYRI-B (Roy et al., 2010; Yang et al., 2015; Zhang, 2008; Kaplan et al., 2020; Yelland et al., 2020), CYRI-A is predicted to contain an amphipathic N-terminal α-helix connected via a flexible linker to a bundle of 12 α–helices forming the Domain of Unknown Function (or DUF1394 domain) (Fig. 2 A). Comparing the amino acid sequence of CYRI-A and CYRI-B shows an 80% sequence identity (Fig. 2 B). The two sequences both share a glutamine residue at the 2nd position thought to be important for myristoylation (Fort et al., 2018) and the two arginine residues at position

bioRxiv preprint doi: https://doi.org/10.1101/2020.12.04.411645; this version posted December 4, 2020. The copyright holder for this preprint (which was not certified by peer review) is the author/funder, who has granted bioRxiv a license to display the preprint in perpetuity. It is made available under aCC-BY-NC-ND 4.0 International license.

159/160 (for CYRI-A) or 160/161 (for CYRI-B) that are essential for active RAC1 binding (Fort et al., 2018). Using an *in vitro* pulldown assay where GST-tagged RAC1 was immobilised onto beads, we showed that the region of CYRI-A that corresponds to the "RAC1 Binding Domain" or RBD of CYRI-B (Fort et al., 2018) (amino acid 29-319) showed a robust interaction with active RAC1 (Fig. 2 C-D). We also performed Surface Plasmon Resonance (SPR) of purified recombinant proteins tagged with MBP immobilised on an SPR chip. Soluble, untagged constitutively active RAC1 Q61L was titrated in at various concentrations. CYRI-B was included as a control and showed a dissociation constant Kd of around 18.3μM (Fig. 2 F), which is similar to the previously reported Kd of around 20μM (Fort et al., 2018). Surprisingly, CYRI-A also interacts with active RAC1 but with a Kd of almost one order of magnitude (2.47μM) lower (Fig. 2 E). Thus CYRI-A is an active RAC1 interacting protein with a higher affinity for active RAC1 than CYRI-B.

bioRxiv preprint doi: https://doi.org/10.1101/2020.12.04.411645; this version posted December 4, 2020. The copyright holder for this preprint (which was not certified by peer review) is the author/funder, who has granted bioRxiv a license to display the preprint in perpetuity. It is made available under aCC-BY-NC-ND 4.0 International license.

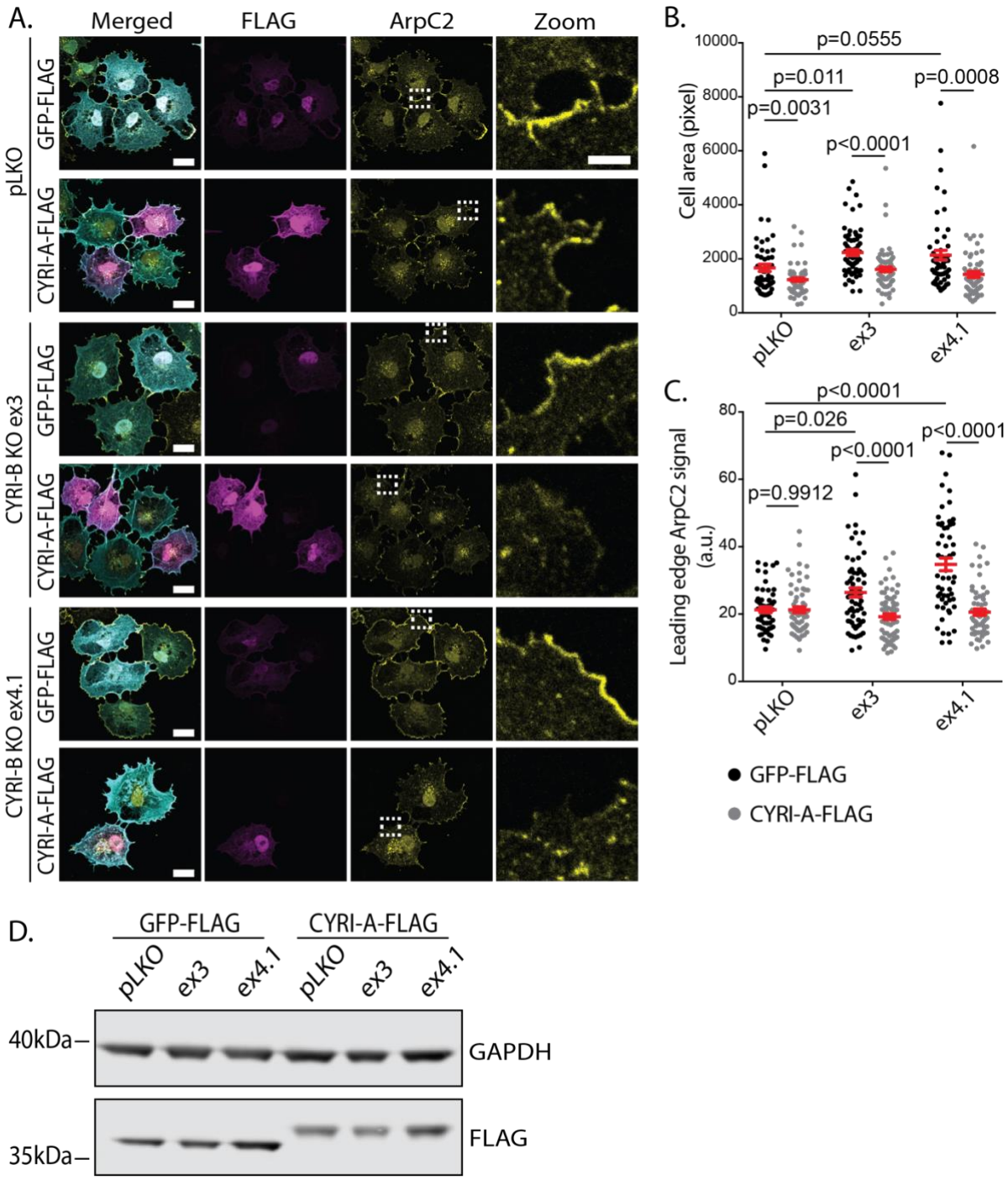

Fig. 1. CYRI-A suppresses cell spreading and leading-edge Arp2/3 complex accumulation in COS-7 cells

A. Immunofluorescence images of COS-7 pLKO (control) and CYRI-B CRISPR lines ex3 or ex4.1 expressing either GFP-FLAG or CYRI-A-FLAG vector (magenta) and stained with Arp2/3 complex (anti-ArpC2, yellow) and phalloidin (cyan) (scale bar = 20μm). Dotted square denotes zooms showing the localisation of Arp2/3 (scale bar = 5μm).

bioRxiv preprint doi: https://doi.org/10.1101/2020.12.04.411645; this version posted December 4, 2020. The copyright holder for this preprint (which was not certified by peer review) is the author/funder, who has granted bioRxiv a license to display the preprint in perpetuity. It is made available under aCC-BY-NC-ND 4.0 International license.

The spreading area and the leading-edge localisation of the Arp2/3 complex reflect the rescue of the CYRI-B deletion phenotype.

B-C. Quantification of the cell spread area and Arp2/3 signal at the leading edge in COS-7 cells expressing either GFP-FLAG or CYRI-A-FLAG construct. Data from at least 10 cells per experiment and 3 independent experiments. Statistical analyses using two-tailed unpaired t-test. Mean ± SEM.

D. Representative western blot shows the relative expression of the overexpressed constructs GFP-FLAG and CYRI-A-FLAG in COS-7. Molecular weight is indicated on the left-hand side.

CYRI-A and CYRI-B cooperatively regulate cancer cell spreading and migration

We next sought to characterise the functional relationship of CYRI-A and CYRI-B in a cellular context where both proteins are expressed at comparable levels to each other. Western blotting of HEK293T cells or COS-7 show that these cells express CYRI-B but either no CYRI-A or at low level, respectively (Fig. S1 B). Using the EMBL-EBI database, we identified that Ewing's sarcoma cell lines and particularly A-673 cells express both isoforms at relatively comparable levels. We confirmed the expression of CYRI-A and B, and the specificity of the antibody in A-673 cells using siRNA or CRISPR-Cas9 (Fig. S1 C, Fig. 3 B). Single knockout of CYRI-A or CYRI-B in A-673 cells resulted in a modest but reproducible effect on the cell shape, with a 10% increase in the number of cells adopting the fast-migrating C-shape, a previously described phenotype (Fort et al., 2018; Yuki et al., 2019) (Fig. 3 A-C). However, when both CYRI-A and CYRI-B were simultaneously deleted (referred to as DBKO for double knockout) that we saw a large increase with 60% of the cells adopting the C-shape morphology. We observed similar effects in cells treated with siRNA (Fig. S1 D-E). DBKO A-673 cells are also accompanied by a 30% increase in the spreading area compared to the control pLKO and single knockout cells. We also measured the migration speed of both CRISPR or siRNA-treated cells on 2D fibronectin substrate and in 3D fibroblast cell-derived matrix (CDM) (Cukierman et al., 2001) (Fig. 3 D-E, Fig. S1 F-G). In all cases, cells lacking both isoforms showed a two-fold increase in their migration speed (0.5μm/min for DBKO vs 0.2μm/min for pLKO on 2D and 0.2μm/min for DBKO vs 0.1μm/min for pLKO in 3D). There are no obvious differences in motility or morphology between cells lacking just CYRI-A or CYRI-B. Re-

bioRxiv preprint doi: https://doi.org/10.1101/2020.12.04.411645; this version posted December 4, 2020. The copyright holder for this preprint (which was not certified by peer review) is the author/funder, who has granted bioRxiv a license to display the preprint in perpetuity. It is made available under aCC-BY-NC-ND 4.0 International license.

introduction of CYRI-A into the DBKO cells reduced the migration speed to basal level (Fig. 3 F). Measuring the collective migration behaviour also showed a faster wound closure rate in the DBKO cells compared to either the control pLKO or the single knockout (Fig. 3 G-H). This is not a consequence of cell proliferation since the DBKO cells are, in fact, proliferating slower than the other cell lines (DBKO slope = 0.11, pLKO and single knockout slope = 0.15) (Fig. 3 I). Overall, these data strongly suggest that CYRI-A and CYRI-B have a compensatory role in regulating cell shape and migration in A-673 cells.

CYRI-A localises to macropinocytic cups

Our results, combined with previous observations (Fort et al., 2018; Yuki et al., 2019) argue that CYRI proteins interact directly with RAC1 and oppose its activity at the cell leading edge. However, almost nothing is known about the cellular localisation or dynamics of CYRI proteins. Fluorescent tagging of CYRIs has proven difficult, as neither N- nor C-terminal tagging preserves their functions (Fort et al, 2018). In an attempt to preserve the N-terminal myristoylation and any role of the N-terminal α-helix, we inserted GFP just after the 16th proline residue of CYRI-A (P16-GFP-CYRI-A) or the 17th proline residue of CYRI-B (P17-GFP-CYRI-B) (Fig. S1 H). Both constructs are able to rescue CYRI-B knockout phenotypes in CRISPR COS-7 cells, suggesting that they are functional (Fig. S1 I-K). We make use of both the COS-7 and HEK293T cell lines for most of our live imaging experiments as these cells are easy for expressing exogenous proteins and imaging. Transiently expressing P16-GFP-CYRI-A in HEK293T and COS-7 cells all results in a striking localisation to many vesicular and occasionally tubular structures (Fig. 4 A-D). The size of the vesicles is around 1μm in diameter, but the length of the tubules can vary from 2 to 8μm. CYRI-A is dynamically localised to vesicles, with resident times of around 50-100s (Fig. 4 C-G).

bioRxiv preprint doi: https://doi.org/10.1101/2020.12.04.411645; this version posted December 4, 2020. The copyright holder for this preprint (which was not certified by peer review) is the author/funder, who has granted bioRxiv a license to display the preprint in perpetuity. It is made available under aCC-BY-NC-ND 4.0 International license.

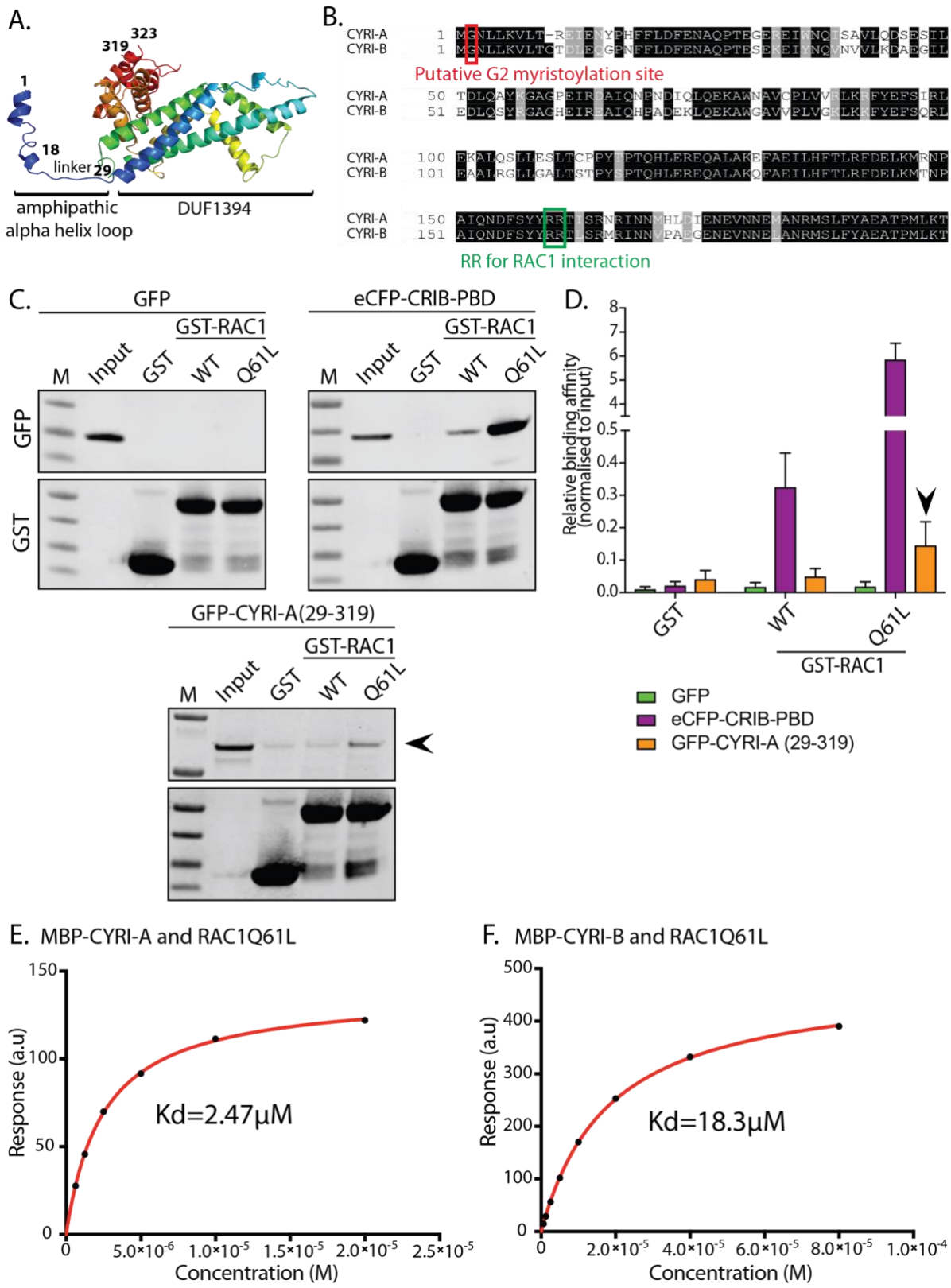

Fig. 2. CYRI-A shares large sequence identity with CYRI-B and also binds active RAC1

bioRxiv preprint doi: https://doi.org/10.1101/2020.12.04.411645; this version posted December 4, 2020. The copyright holder for this preprint (which was not certified by peer review) is the author/funder, who has granted bioRxiv a license to display the preprint in perpetuity. It is made available under aCC-BY-NC-ND 4.0 International license.

A. The predicted crystal structure of CYRI-A by I-TASSER. The protein is composed of one amphipathic α-helix connected to a Domain of Unknown Function (DUF) 1394 via a flexible linker. Numbers represent the amino acid position.

B. Multiple sequence alignment using Clustal Omega of mouse CYRI-A and CYRI-B shows an 80% sequence identity. Highlighted in red is the 2nd Glycine (G2) residues that are thought to be a myristoylation site. Highlighted in green are two conserved arginine residues (RR) that are important for mediating active RAC1 binding.

C. GST-Trap pulldown assay of GST or GST-RAC1 (WT or Q61L) with lysate from COS-7 cells containing GFP (negative control), eCFP-CRIB-PBD (positive control) or GFP-CYRI-A (29-319) (RBD). Membranes were blotted with anti-GFP and anti-GST. Signals were normalised to the input. The black arrow shows the detected interaction between GFP-CYRIA (29-319) and GST-RAC1 Q61L.

D. Graph shows the quantification of C) from at least 3 independent experiments. Mean ± SEM. Black arrowhead points to the increased signal between the RBD and active RAC1.

E-F. Surface Plasmon Resonance (SPR) experiment between CYRIs and RAC1Q61L. MBP-tagged full-length CYRI-A or CYRI-B is immobilised on the chip surface while increasing levels of untagged full-length RAC1 Q61L is in the mobile phase. The calculated dissociation constant (Kd) of CYRI-A is 2.47μM and of CYRI-B is 18.3μM.

bioRxiv preprint doi: https://doi.org/10.1101/2020.12.04.411645; this version posted December 4, 2020. The copyright holder for this preprint (which was not certified by peer review) is the author/funder, who has granted bioRxiv a license to display the preprint in perpetuity. It is made available under aCC-BY-NC-ND 4.0 International license.

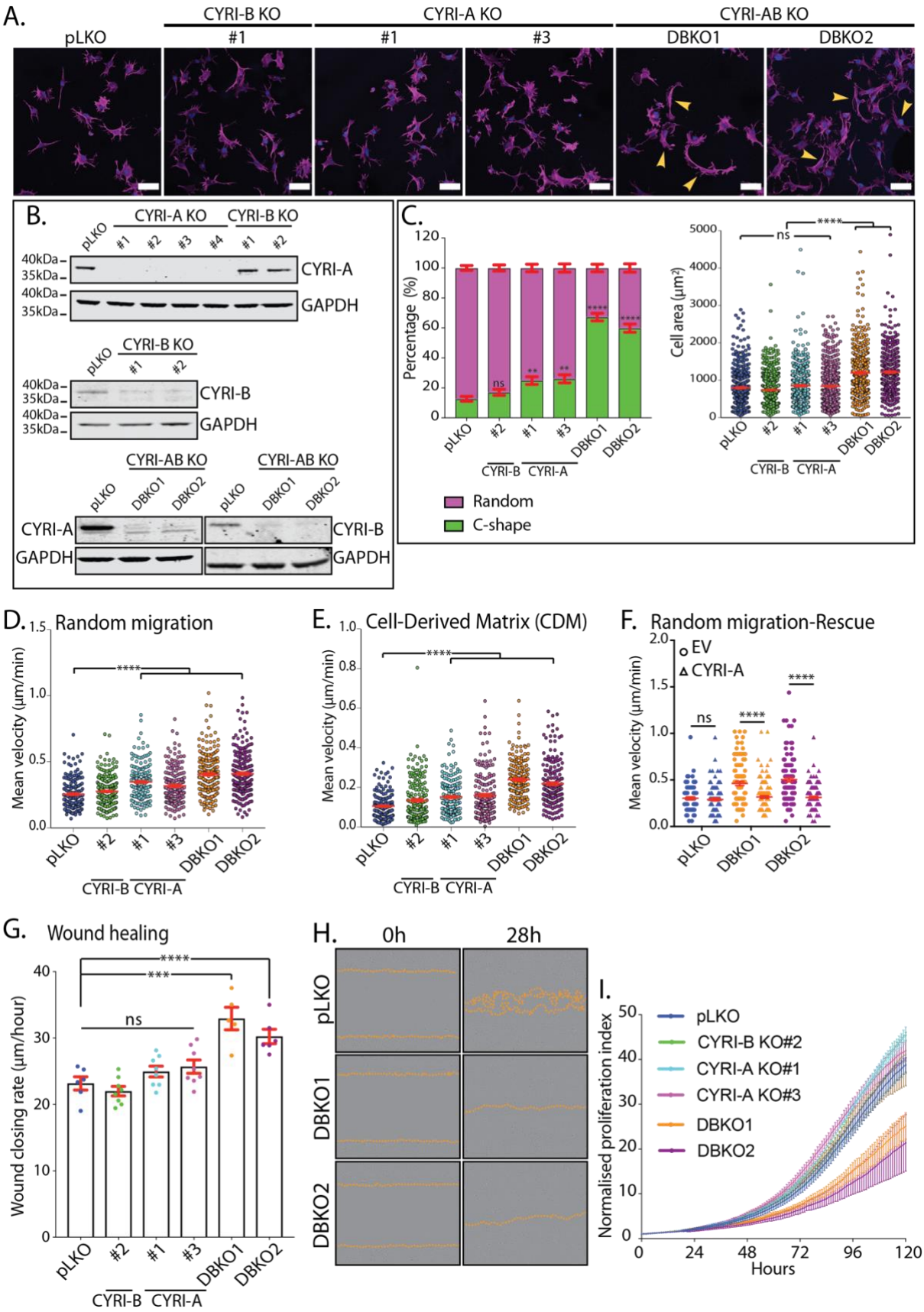

Fig. 3. CYRI-A and CYRI-B cooperatively regulate cell shape and migration

bioRxiv preprint doi: https://doi.org/10.1101/2020.12.04.411645; this version posted December 4, 2020. The copyright holder for this preprint (which was not certified by peer review) is the author/funder, who has granted bioRxiv a license to display the preprint in perpetuity. It is made available under aCC-BY-NC-ND 4.0 International license.

A. Immunofluorescence images of control (pLKO), single knockout and double knockout (DBKO) of CYRIs in A-673 cells. Cells stained for phalloidin (magenta) and DAPI (blue). Yellow arrows indicate C-shape cells. Scale bar = 50μm.

B. Western blots showing the efficiency of single and double knockout of CYRIs.

C. Quantification of the cell shape (left) and cell area (right) of A) from at least 50 cells per experiment.

D-E. Migration analysis of CYRI CRISPR cells on 2D fibronectin substrate or in 3D cell-derived matrix.

F. Re-expression of CYRI-A in the DBKO cells reduces their speed to the original values, while did not affect the control pLKO cells.

G-H. Wound healing assay comparing between the control pLKO, single knockout and double knockout CYRI cells.

I. Proliferation assay of the control pLKO, single knockout and double knockout of CYRIs in A-673 cells.

Data from at least 3 independent experiments. Mean ± SEM. ANOVA with Tukey's multiple comparisons. ns = $p>0.05$, * $p<0.05$, ** $p<0.01$, *** $p<0.001$, **** $p<0.0001$.

Interestingly, we also observe a diffused localisation of CYRI-A proximal to the cell leading edge in COS-7, and seems to be recruited to the forming endocytic cups (Fig. 4 D, arrowheads). In contrast to the dynamic behaviour of CYRI-A, the signal of CYRI-B in COS-7 cells decorating tubules and vesicles is much more stable (Fig. S2 A). The size of CYRI-B positive vesicles is smaller than CYRI-A, with an average of 0.5μm, while tubular structures are more prominent which can reach up to 20μm (Fig. S2 B). These observations not only confirm the ability of CYRIs to interact with the cell membrane but also suggest for the first time a potential difference between CYRI-A and CYRI-B in membrane kinetics.

The prominent localisation of CYRIs and the size of these vesicles, in particular CYRI-A, begs the question about the nature of these structures. We performed dual colour live imaging of COS-7 cells co-expressing the internal GFP-tagged CYRI construct and mCherry-tagged RAB5A as a marker for early endosomes. Interestingly, CYRI-A demonstrates a transient colocalization with RAB5A (Fig. 4 E-G). As the vesicles formed, CYRI-A is quickly recruited and remains on the vesicles for around 50s before RAB5A signal appears. The gradual appearance of RAB5A

bioRxiv preprint doi: https://doi.org/10.1101/2020.12.04.411645; this version posted December 4, 2020. The copyright holder for this preprint (which was not certified by peer review) is the author/funder, who has granted bioRxiv a license to display the preprint in perpetuity. It is made available under aCC-BY-NC-ND 4.0 International license.

coincides with the gradual loss of the CYRI-A signal, which takes another 50s (Fig. 4 G). RAB5A remains on the vesicles as they are being transported further into the cells. This confirmed that CYRI-A-positive vesicles are indeed part of the endocytic trafficking network and positioned CYRI-A upstream of RAB5A. We also verified this observation in HEK293T cells (Fig. S2 C-E). On the other hand, CYRI-B remained relatively evenly distributed on vesicles and tubules over these timescales (Fig. S2 F-G). Due to the relatively large size of many of the CYRI-A vesicles, we speculated that they could be macropinosomes (Canton, 2018; Swanson and Watts, 1995). Using fluorescent dextran 70kDa as a marker for fluid-phase uptake, we found that 75% of CYRI-A positive vesicles in COS-7 (Fig. 4 H-I) and almost 100% in both HEK293T and CHL-1 cells contained dextran (Fig. S2 H-M). Those that are dextran negative tend to be much smaller and are significantly less frequent. The size of these dextran containing vesicles (0.6-1μm on average) is within the range of those previously described in Fig. 4 A-D and is consistent with macropinosomes (Canton, 2018; Swanson and Watts, 1995). We tested the colocalization of CYRI vesicles with other classical endocytosis pathways including clathrin-mediated endocytosis (CLC15), caveolin-mediated endocytosis (CAV1) and ARF1-dependent endocytosis (ARF1) (Fig. S3 A-D) but found no clear colocalization with these markers at any of the observed events. Overall, these data provide evidence that CYRIs are involved in macropinocytosis. CYRI-B is not very dynamic, but CYRI-A is recruited early to nascent macropinosomes, prior to RAB5A recruitment.

CYRI-A regulates macropinosome maturation and form a feedback loop with actin

Actin polymerisation shapes the macropinocytic cup in the early stages (Bloomfield and Kay, 2016; Condon et al., 2018) and CYRI proteins are recruited by active RAC1 during actin polymerisation in lamellipodia (Fort et al., 2018), so we hypothesized that CYRI-A and actin could coordinate their activities during macropinocytosis. Co-transfecting COS-7 cells with LifeAct-RFP along with the internally GFP-tagged CYRI-A shows co-localisation between actin and CYRI-A but not with GFP alone (Fig. 5 A). Tracking the signal intensity between actin and CYRI-A, it was apparent that actin accumulation at the macropinosome preceded CYRI-A accumulation (Fig. 5 B). Actin is dynamic and drives the early stages of macropinocytic cup formation (Mooren et al., 2012; Bloomfield, 2016; Yoshida, 2009). In COS-7 cells, we often observe the

bioRxiv preprint doi: https://doi.org/10.1101/2020.12.04.411645; this version posted December 4, 2020. The copyright holder for this preprint (which was not certified by peer review) is the author/funder, who has granted bioRxiv a license to display the preprint in perpetuity. It is made available under aCC-BY-NC-ND 4.0 International license.

actin signal increases and decreases multiple times around vesicles. Each time the actin signal increases, it is sharply followed by the increase of the CYRI-A signal (Fig. 5 B, graph) then both signals decrease, suggesting sequential recruitment. We verified this observation in HEK293T cells (Fig. 5 C-D). Similarly, CYRI-A signal coincides with the quick decrease in the actin signal and then both signals level off. On average, the actin signal persists on the vesicles for around 36s before the CYRI-A signal becomes detectable. CYRI-A and actin coincide for about another 54s on average before both decreases, similar to the lifetime of CYRI-A on these vesicles before RAB5A appears (Fig. S2 E). To directly compare the effects of CYRIs on the closure and maturation of macropinocytic cups and the resident time of actin on these vesicles, we co-expressed LifeAct-RFP and either GFP alone or the internal GFP-CYRI-A constructs in COS-7 cells that have been depleted of both CYRI-A and CYRI-B using siRNA (DBKD for double knockdown) (Fig. 5 E-G). As expected, DBKD COS-7 cells are flat with relatively nondynamic lamellipodia. Counting the number of actin-positive vesicles formed shows that cells expressing GFP form significantly fewer vesicles (~4 vesicles/cell) compared to cells rescued with the internal GFP-CYRI-A (~65 vesicles/cell). Measuring the resident time of actin reveals that vesicles that are positive for CYRI-A have shorter actin lifetime (~92s) compared to those that are negative (~212s). Indeed, DBKD cells uptake significantly less dextran 70kDa than control cells after 30min of incubation (Fig. 5 H-I). This suggests that CYRI-A suppresses the actin signal around macropinosomes to accelerate their maturation process. To query the possible actin-dependence of CYRI-A localisation, we treated COS-7 and HEK293T cells expressing both CYRI-A and LifeAct with 1μM of Latrunculin A, which binds to monomeric actin and prevents actin polymerisation (Yarmola et al., 2000) (Fig. 5 J). Within 30s of addition, the actin cytoskeleton collapsed, but CYRI-A vesicles were still frequently observed, even without any obvious membrane ruffles. This suggests that CYRI-A does not directly depend on actin for its localisation. However, Latrunculin A decreases the lifetime of CYRI-A significantly, from 100s to about 50s in COS-7 and from around 50s to around 20s in HEK293T cells (Fig. 5 J), suggesting a feedback loop between actin and CYRI-A.

bioRxiv preprint doi: https://doi.org/10.1101/2020.12.04.411645; this version posted December 4, 2020. The copyright holder for this preprint (which was not certified by peer review) is the author/funder, who has granted bioRxiv a license to display the preprint in perpetuity. It is made available under aCC-BY-NC-ND 4.0 International license.

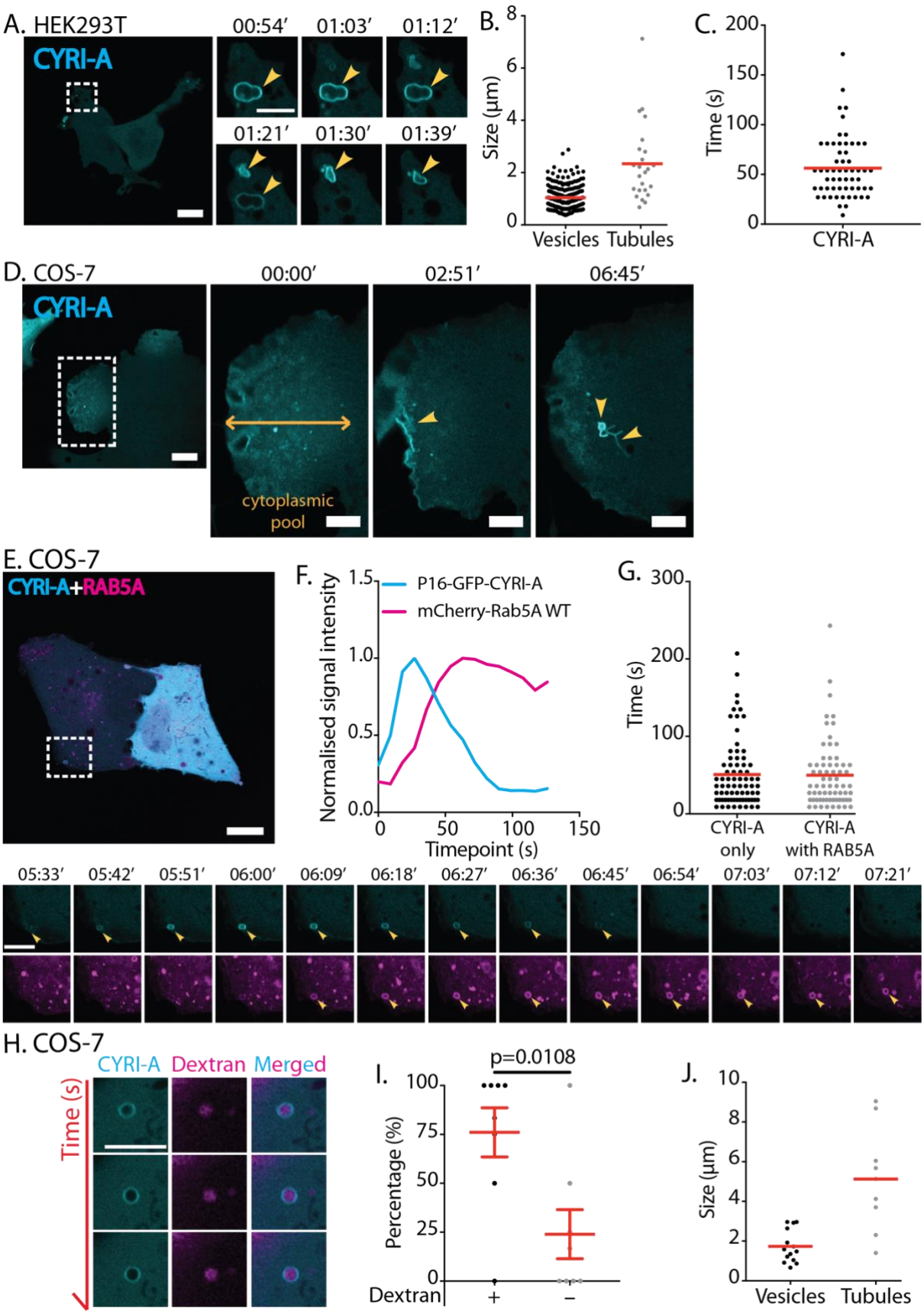

bioRxiv preprint doi: https://doi.org/10.1101/2020.12.04.411645; this version posted December 4, 2020. The copyright holder for this preprint (which was not certified by peer review) is the author/funder, who has granted bioRxiv a license to display the preprint in perpetuity. It is made available under aCC-BY-NC-ND 4.0 International license.

Fig. 4. (See video 1 to 4) CYRI-A localises to large macropinocytic cup-like structure prior to RAB5A recruitment

A-C. CYRI-A in HEK293T (scale bar = 20μm) (N=204 events in 18 cells for vesicles and N=24 events in 10 cells for tubules) decorates structures resembling macropinocytic cups (yellow arrows, diameter ranging from 0.4 to 2.9μm, scale bar = 5μm). Tubules with lengths ranging from 0.7 to 7μm. The average lifetime of CYRI-A on cups in HEK293T is about 50s (N=58 events in 5 cells). Red lines represent the average value.
D. Still images of COS-7 cells (scale bar = 20μm) expressing CYRI-A showing the diffused pool of CYRI-A (yellow double arrow) near the leading. Dotted square is shown as time sequence on the right (scale bar = 5μm).
E. Time-lapse of COS-7 cells expressing P16-GFP-CYRI-A (cyan) and mCherry-RAB5A (magenta). CYRI-A is enriched around vesicular or tubular structures with a transient colocalization with RAB5A. Scale bar = 20μm (full size) or 5μm (zoom).
F-G. Quantification showing the time sequence of CYRI-A and RAB5A recruitment to the macropinocytic cups (CYRI-A only N=75 events in 8 cells; CYRI-A with RAB5A N=68 events in 8 cells).
H-J. Dextran incorporation assay shows CYRI-A decorates dextran-positive vesicles (scale bar = 5μm). Quantification of the percentage of CYRI-A positive vesicles that contain dextran (N=9 cells) and the size of these vesicles and tubules (vesicles N=15 events in 7 cells; tubules N=10 events in 7 cells). Two-tailed unpaired t-test.

Since Latrunculin A has been shown to activate the Scar/WAVE complex by an unknown mechanism (Millius et al., 2009; Weiner, 2007), which could potentially influence the behaviour of CYRI-A, we reconfirmed our observation using Cytochalasin D, which caps the F-actin and prevents the addition of new actin monomers (Schliwa, 1982). Upon the addition of 1μM Cytochalasin D, a similar response was observed and the lifetime of CYRI-A on the vesicles was consistently decreased to similar values as in the case of Latrunculin A (Fig. 5 K). Overall, these data suggest that CYRI-A is recruited to macropinosomes to oppose positive signals that enhance the actin network such as RAC1 and Scar/WAVE. CYRI-A's lifetime at the macropinosomes but not its recruitment is actin-dependent. This fits with our hypothesis for CYRI-A as a local inhibitor of actin assembly at macropinosomes, which drives the maturation process.

bioRxiv preprint doi: https://doi.org/10.1101/2020.12.04.411645; this version posted December 4, 2020. The copyright holder for this preprint (which was not certified by peer review) is the author/funder, who has granted bioRxiv a license to display the preprint in perpetuity. It is made available under aCC-BY-NC-ND 4.0 International license.

CYRI-A regulates actin dynamics through suppressing active RAC1 activity at macropinocytic cups

Direct observation of the spatiotemporal localisation of RAC1 at macropinocytic cups is limited. We thus sought to follow CYRI-A and wild-type RAC1 *in cellulo* to capture their dynamics. Cells overexpressing GFP-tagged RAC1 are broadly spread and display membrane ruffles (Fig. 6 A). RAC1 signal enriches at the edge of the plasma membrane, especially in ruffles and folds (Fig. 6 A). These ruffles fold onto themselves and form macropinosomes (Fig. 6 A, yellow arrowhead). Importantly, CYRI-A signal is diffuse during the very early phase where the RAC1 signal was first observed. However, as the RAC1 signal gradually accumulates (for around 50s), it is followed by a sharp increase in the CYRI-A signal (Fig. 6 B-C). The increase of CYRI-A signal precedes the immediate drop in RAC1 signal, then both signals disappear, which takes another 50s, as the macropinocytic cup matures. The timing of RAC1 accumulation matches closely to the timing of filamentous actin accumulation on these cups (Fig. 5 B-C), suggesting a mechanistic connection between CYRI-A, RAC1 and actin. We next examined the specific localisation of active RAC1 relative to CYRI-A, using the CFP-tagged Pak Binding Domain (PBD) (Fig. 6 D-E). The PBD signal accumulates as the cups mature and prior to the point where PBD is accompanied by a sharp burst of CYRI-A signal before both dissipate. It is important to emphasize that all of these events happen locally on the macropinocytic cups as they are forming with a high degree of spatiotemporal control. We queried whether CYRI-A's ability to bind active RAC1 is important for its recruitment to nascent macropinosomes by using a RAC1-binding defective mutant (Yelland et al., 2020) with arginine 159 and 160 mutated to aspartic acid (P16-mCh-CYRI-A-RRDD). We co-transfected COS-7 or HEK293T cells with the wild-type P16-GFP-CYRI-A and either the wild-type or the mutant RRDD construct of P16-mCherry-CYRI-A (Fig. 6 F-K, Fig. S3 G-H). In all cell types tested, GFP-tagged and mCherry-tagged wild-type CYRI-A show close colocalization at every endocytic event captured. In contrast, mutant CYRI-A did not co-localise with wild-type CYRI-A on any of these endocytic events. Overall, these data strongly suggest that CYRI-A is locally recruited to the macropinocytic cups to suppress actin signalling by responding to the presence of active RAC1 at a certain threshold level.

bioRxiv preprint doi: https://doi.org/10.1101/2020.12.04.411645; this version posted December 4, 2020. The copyright holder for this preprint (which was not certified by peer review) is the author/funder, who has granted bioRxiv a license to display the preprint in perpetuity. It is made available under aCC-BY-NC-ND 4.0 International license.

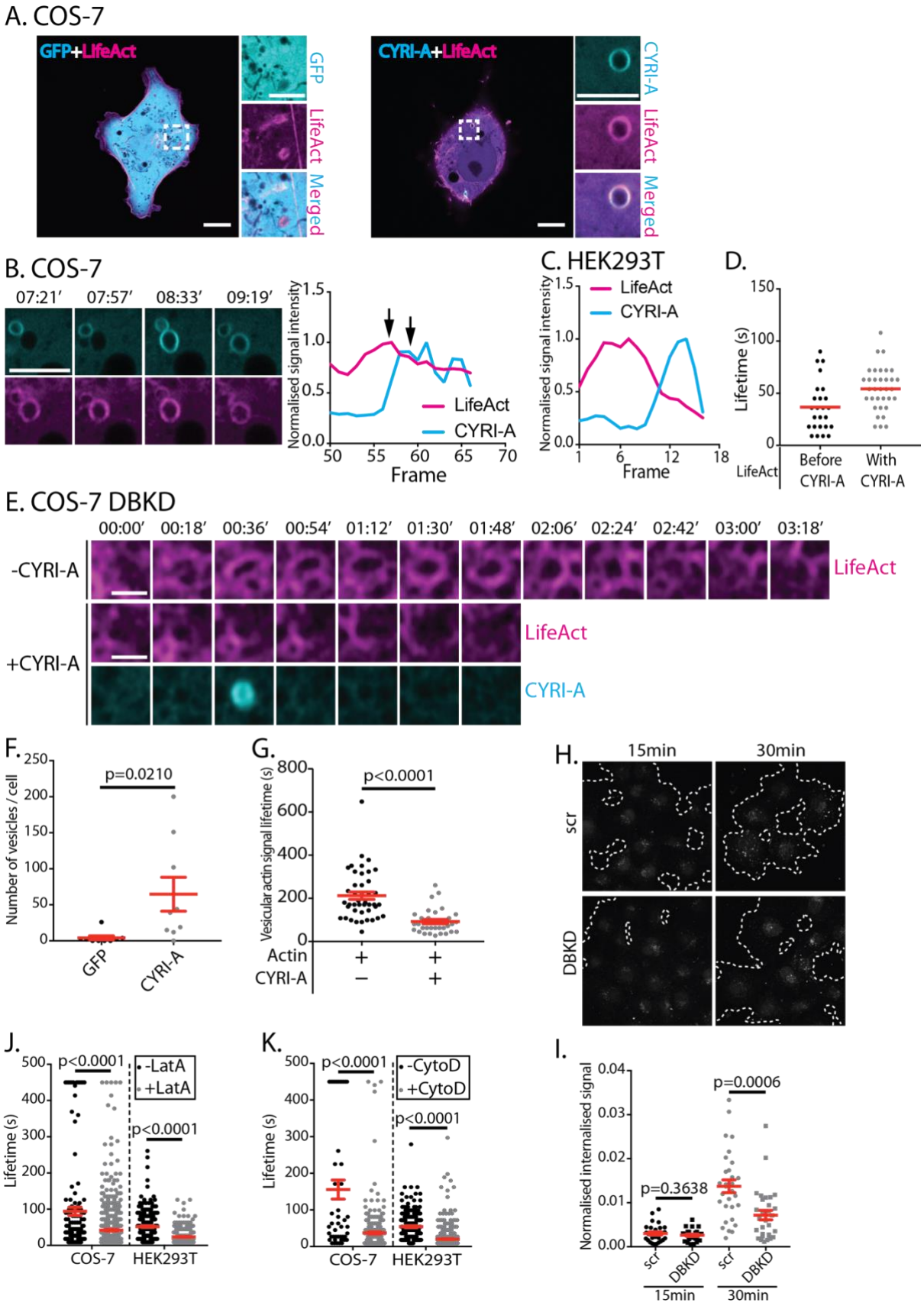

bioRxiv preprint doi: https://doi.org/10.1101/2020.12.04.411645; this version posted December 4, 2020. The copyright holder for this preprint (which was not certified by peer review) is the author/funder, who has granted bioRxiv a license to display the preprint in perpetuity. It is made available under aCC-BY-NC-ND 4.0 International license.

Fig. 5. (See video 5 to 10) CYRI-A regulates actin signal at the macropinocytic cups and macropinosome maturation

A. Still images of COS-7 cells expressing either GFP (negative control) or CYRI-A and LifeAct-RFP. CYRI-A shows a strong colocalization with actin at macropinosomes. Scale bar = 10μm for full-sized image and 5μm for zooms.

B. Time sequence images showing the dynamics of CYRI-A and actin at the macropinosome in COS-7 cells. The graph shows the normalised signal intensities over time. Black arrows show the two peaks of the actin and the CYRI-A signal. Scale bar = 5μm.

C. The line graph shows the normalised signal intensities over time between CYRI-A and LifeAct signal in HEK293T cells.

D. Quantification showing the lifetime of actin before and after CYRI-A is recruited in HEK293T cells (Before CYRI-A: N=25 events in 10 cells, With CYRI-A: N=34 events in 10 cells). Red lines indicate the average value. Scale bar = 10μm for full-sized image and 5μm for zooms.

E-G. Time sequence images showing the lifetime of actin on the cups with or without the presence of CYRI-A in CYRI DBKD COS-7 cells. Scale bar = 1μm. Quantification of the number of actin-positive cups between cells with or without the internally GFP-tagged CYRI-A construct (N=9 cells) (F). Quantification of the lifetime of the actin signal on cups that are negative or positive for CYRI-A signal (Actin alone: N=43 events in 9 cells; Actin with CYRI-A: N=33 events in 8 cells).

H. Macropinocytosis assay in siRNA-treated COS-7 cells. Scr = scramble, DBKD = double knockdown.

I. Quantification of the macropinocytic index of H. Data are from at least 10 different fields of view per experiment from a total of 3 independent experiments. Statistical analysis using two-tailed unpaired t-test. Mean ± SEM.

J-K. Graphs show the lifetime of CYRI-A on macropinosomes in the absence or presence of Latrunculin A (LatA) or Cytochalasin D (CytoD) in COS-7 and HEK293T cells. Data from 3 independent experiments. Mean ± SEM. Statistical analysis using two-tailed unpaired t-test.

bioRxiv preprint doi: https://doi.org/10.1101/2020.12.04.411645; this version posted December 4, 2020. The copyright holder for this preprint (which was not certified by peer review) is the author/funder, who has granted bioRxiv a license to display the preprint in perpetuity. It is made available under aCC-BY-NC-ND 4.0 International license.

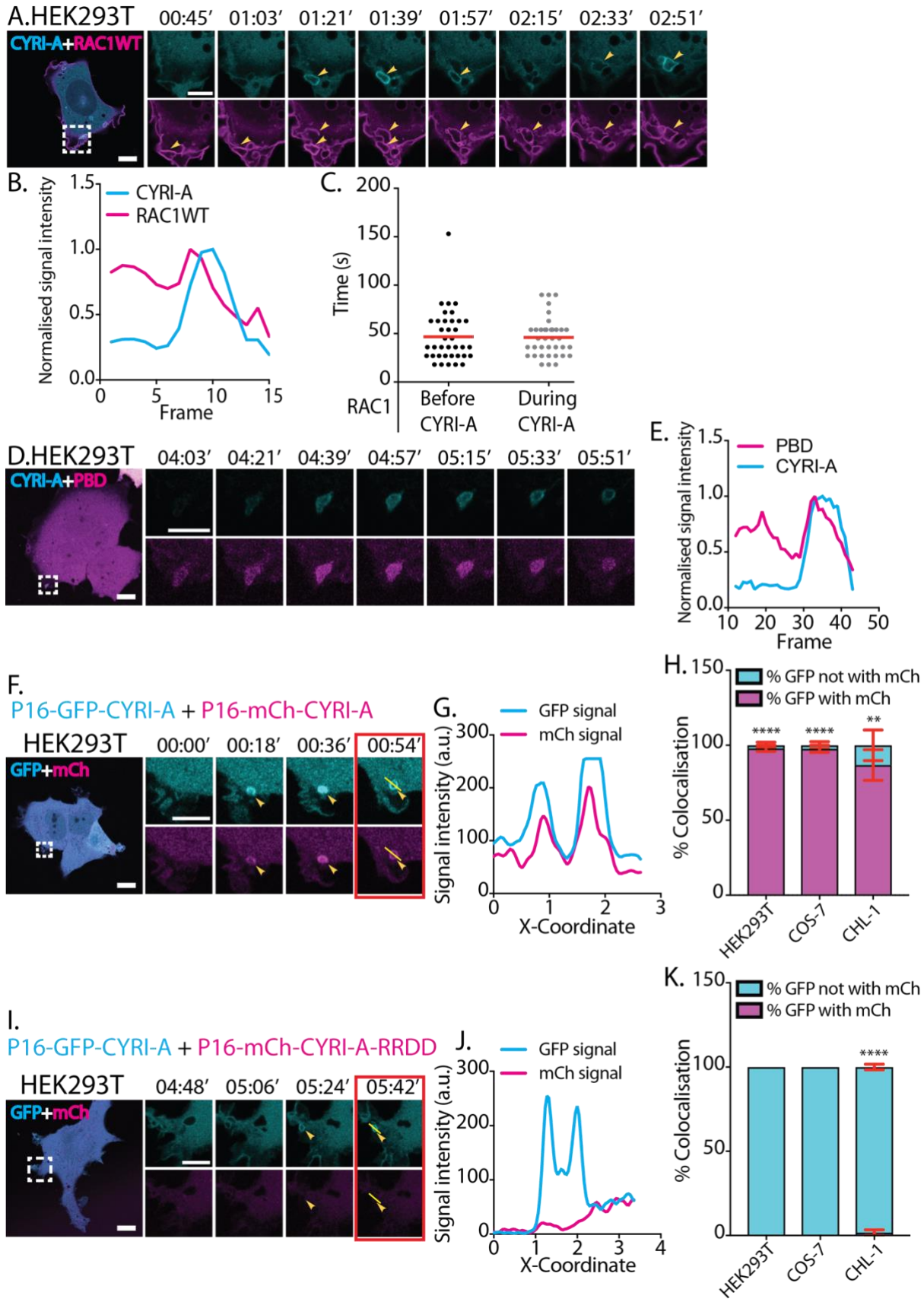

bioRxiv preprint doi: https://doi.org/10.1101/2020.12.04.411645; this version posted December 4, 2020. The copyright holder for this preprint (which was not certified by peer review) is the author/funder, who has granted bioRxiv a license to display the preprint in perpetuity. It is made available under aCC-BY-NC-ND 4.0 International license.

Fig. 6. (See video 11 to 14) CYRI-A is recruited to the macropinocytic cups by active RAC1

A-C. Time sequence images of HEK293T cell expressing P16-mCherry-CYRI-A and GFP-RAC1 WT. (B) shows the normalised signal intensity of the sequential event between RAC1 and CYRI-A. (C) Quantification of the lifetime of RAC1 signal on the macropinosomes (N=37 events in 4 cells). Scale bar = 10μm for full-sized image and 5μm for zooms.

D-E. Time sequence images of HEK293T cell expressing P16-GFP-CYRI-A and CFP-PBD. The graph shows the normalised signal intensities of CYRI-A and PBD over time. Scale bar = 10μm for full-sized image and 5μm for zooms.

F-K. Time sequence images of HEK293T cells expressing either WT or RRDD mutant of mCherry-CYRI-A with the WT GFP-CYRI-A (F, I). Line graphs show the colocalization of the signals between the two fluorescent constructs (G, J). Bar charts show the quantification of the percentage of colocalization events (N=5 cells) (H, K). Scale bar = 10μm for full-sized image and 5μm for zooms. Statistical analysis using two-tailed unpaired t-test. **$p<0.01$, ****$p<0.0001$.

The recruitment of CYRI-A to macropinosomes is downstream of and dependent on PI3K signalling

PI-3 Kinase signalling plays an important role during macropinocytosis formation, as PIP3 production has been shown to recruit many RAC1 GEFs (Araki et al., 2007; Bloomfield and Kay, 2016; Bohdanowicz and Grinstein, 2013; Campa et al., 2015). We visualised phosphatidylinositol (3,4,5)-trisphosphate (PIP3) using two independent reporters PH-Grp1 (Kavran et al., 1998; Lai et al., 2013) and PH-Btk (Araki et al., 2007; Varnai et al., 2005) along with CYRI-A in HEK293T cells. Remarkably, the PIP3 signal appeared for approximately 38 to 44s and peaked before the CYRI-A signal slowly appeared (Fig. 7 A-F). Similar observations were made in COS-7 cells, even though expressing the PIP3 reporters in this cell line tended to form long tubules clumping together which made spatiotemporally resolving them more difficult (Fig. S3 I-N). Our observations fit nicely with the consensus model where PIP3 is generated likely to recruit RAC1 GEFs, which activates RAC1 and drives actin polymerisation (Bloomfield and Kay, 2016; Buckley and King, 2017; Swanson and Watts, 1995) and the recruitment of CYRI-A can dampen down this signalling

bioRxiv preprint doi: https://doi.org/10.1101/2020.12.04.411645; this version posted December 4, 2020. The copyright holder for this preprint (which was not certified by peer review) is the author/funder, who has granted bioRxiv a license to display the preprint in perpetuity. It is made available under aCC-BY-NC-ND 4.0 International license.

pathway. Blocking PI3K activity using 20μM LY294002 almost completely disrupts the recruitment of CYRI-A to the vesicles in COS-7 (Fig. 7 G-H). It is interesting to note that cells treated with LY294002 still retain membrane ruffles (Araki et al., 1996), but both diffused and localised recruitment of CYRI-A, is completely abolished. This fits in with a previous observation that LY294002 blocks the resolution of macropinosomes (Araki et al., 1996). Interestingly, when we label the plasma membrane in HEK293T cells using mScarlet-Lck (Chertkova et al., 2020), we observe that the plasma membrane invaginates for 50s before CYRI-A is recruited (Fig. S3 O-P). Just before the completion of the vesicles, CYRI-A signal appears coincident with the budding off of the vesicles into the cytoplasm. This suggests CYRI-A signal is distinct from the very early step during the invagination process and perhaps also hints to its role in the resolution of the macropinocytic cup into a vesicle. Overall, the function of CYRI-A is downstream of and strongly dependent on PI3K-PIP3 activity.

CYRI proteins affect the trafficking of integrin α5β1

One of the major cargoes of macropinocytic uptake is integrins (Gu et al., 2011; Caswell, 2009; De Franceschi, 2015). Furthermore, the broad spread lamellipodial phenotype of CYRI-A/B knockout cells (DBKO) suggested a possible enhancement of spreading due to a change in adhesion. We hence queried whether CYRI proteins could impact on the adhesion and integrin trafficking. Using the Xcelligence adhesion assay system based on electrical impedance, we found that CYRI DBKO A-673 cells spread around 2-fold faster than single knockouts or controls (Fig. 8 A-B). Flow cytometry analysis revealed an almost 50% increase in the surface expression of integrin α5 and β1 in the two DBKO A-673 cell lines compared to the control pLKO (Fig. 8 C-D). Western blotting shows a minor but consistent increase of the total level of integrin α5 and β1 while qRT-PCR analysis shows no obvious change in their mRNA levels (Fig. 8 E-F). We detected a similar increase for the active integrin α5 using the SNAKA51 antibody with flow cytometry, but no change for the level of the membrane metalloprotease MT1-MMP (Fig. S4 A-B). Immunofluorescence analysis revealed a significant increase in both the area of adhesion clusters as well as their number per cell in the DBKO cells compared to the controls (Fig. 8 G-H, Fig. S4 C-E). Overexpression of CYRI-A in the DBKO cells rescued these phenotypes (Fig. 8 I-

bioRxiv preprint doi: https://doi.org/10.1101/2020.12.04.411645; this version posted December 4, 2020. The copyright holder for this preprint (which was not certified by peer review) is the author/funder, who has granted bioRxiv a license to display the preprint in perpetuity. It is made available under aCC-BY-NC-ND 4.0 International license.

J). Overall, we find that loss of both CYRI isoforms in A-673 cells led to the enhanced display of surface integrins, suggesting a defect in their intracellular trafficking.

Integrin α5 and β1 are localised to CYRI-positive cups and vesicles

Since CYRIs are involved in the forming of macropinosomes and macropinocytosis is a major effector of bulk internalisation of integrins (Gu et al., 2011; Caswell, 2009; De Franceschi, 2015), we next asked whether integrins co-localise with CYRI proteins at these structures. We first co-expressed a mApple-tagged integrin α5 construct along with the internally tagged P16-GFP-CYRI-A or P17-GFP-CYRI-B in COS-7 (Fig. 9 A-B) or HEK293T cells (Fig. S4 F). Integrin α5 decorated many intracellular vesicles, including CYRI-A-positive macropinocytic cups formed near the edge of the cells (Fig. 9 A). CYRI-B could also be seen decorating endocytic tubules emanating from the tip of filopodia-liked protrusions or from the side of the cell (Fig. 9 B). Endogenous localisation of integrins also colocalises with CYRI-A and CYRI-B-positive macropinocytic cup-like structures in COS-7 (Fig. 9 C-H) as well as in the DBKO A-673 cells (Fig. S4 G-J).

Increased surface presentation of integrin α5 and β1 suggested a potential defect in internalisation, perhaps due to the requirement for CYRI proteins in the resolution of macropinocytic structures. To address this, we performed an internalisation assay of the active integrin α5. After 30min of induction, we observed a significant increase in the internalised signal particularly in the control cells (Fig. 9 I-J). Also, the control pLKO cells have a much stronger intracellular signal compared to the DBKO cells, suggesting that a higher level of active integrins were internalised. Overall, our data support a novel function of CYRIs in cooperatively regulating the trafficking of integrin α5β1 through the enhancement of actin dynamics during macropinocytosis to allow the efficient internalisation of surface integrins.

bioRxiv preprint doi: https://doi.org/10.1101/2020.12.04.411645; this version posted December 4, 2020. The copyright holder for this preprint (which was not certified by peer review) is the author/funder, who has granted bioRxiv a license to display the preprint in perpetuity. It is made available under aCC-BY-NC-ND 4.0 International license.

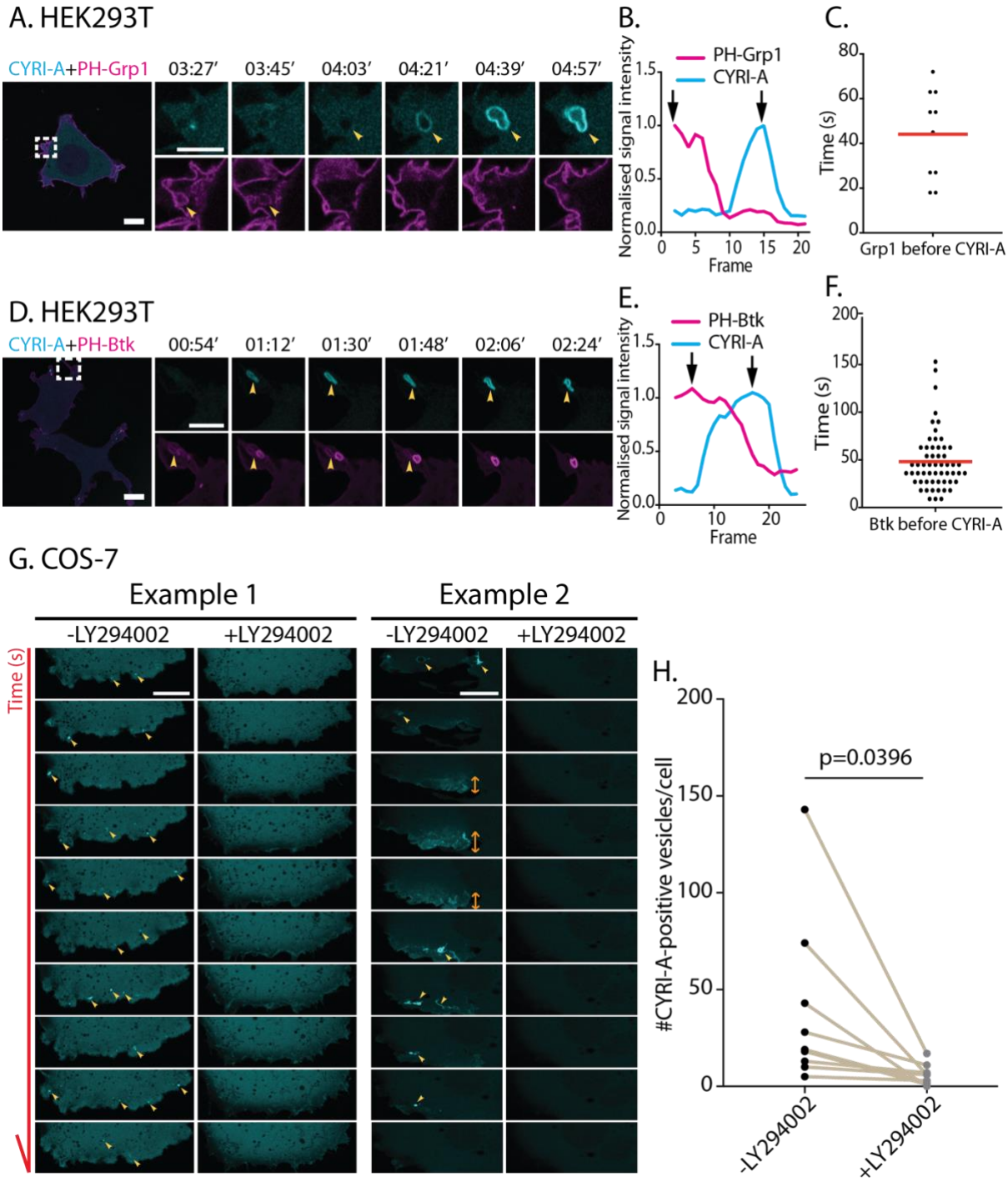

Fig. 7. (See video 15 to 18) CYRI-A's recruitment to the macropinocytic cups is downstream of and dependent on PI3K signalling

A-F. HEK293T cells were co-transfected with mCherry-tagged CYRI-A and either GFP-PH-Grp1 or GFP-PH-Btk as specific markers for Phosphatidylinositol-3,4,5-phosphate (PIP3) (A, D). Line graphs show the sequential events between PIP3 reporters and CYRI-A (B, E). Scattered plots show the average lifetime of PIP3 reporter signal before CYRI-A is recruited to the macropinosomes (Grp1: N=9 events in 3 cells; Btk1:

bioRxiv preprint doi: https://doi.org/10.1101/2020.12.04.411645; this version posted December 4, 2020. The copyright holder for this preprint (which was not certified by peer review) is the author/funder, who has granted bioRxiv a license to display the preprint in perpetuity. It is made available under aCC-BY-NC-ND 4.0 International license.

N=57 events in 6 cells). Red lines represent the average value. Scale bar = 10μm for full-sized images and 5μm for zooms.

G-H. Time sequence images showing COS-7 cells expressing GFP-tagged CYRI-A before and after the addition of 20μM of LY294002. Quantification shows a significant decrease in the number of vesicles formed over time (N=9 cells). Scale bar = 10μm. Statistical analysis using paired t-test.

CYRI DBKO A-673 cells are more invasive and resistant to anoikis due to the increased level of surface integrins

Increased level of α5 and β1 integrins have been associated with increased invasiveness and survival of multiple types of cancer (Bianchi-Smiraglia et al., 2013; Clark, 2005; Mierke, 2011; Nam et al., 2010; Paul et al., 2015). Building on from these observations and our migration data (Fig. 3 D-H, Fig. S1 F-G), we decided to test the invasive capacity of the CYRI DBKO A-673 cells using an organotypic assay where cells invade into native collagen plugs (Timpson et al., 2011). Indeed, loss of CYRI proteins significantly increased invasion (Fig. 10 A-B). The invasion index (area of invading cells divided by the total area of the collagen plug) of the DBKO cells (~10%) is almost 3 times higher than that of the control (~3%). Blocking the activity of the integrin α5β1 using the blocking antibody IIA1 dramatically reduced the invasion of the DBKO cells but not the control into collagen-Matrigel-fibronectin (CMF) plugs in inverted invasion assays (Fig. 10 C-D). Individually inhibiting each subunit with specific blocking antibodies also results in the same reduction (Fig. S5 A-B). On a 2D surface, pre-treating cells with IIA1 blocking antibody significantly reduces their ability to adhere and spread on fibronectin matrix (Fig. S5 C-D). This suggests that in CYRI DBKO cells, integrins play a crucial role in regulating the cell shape and adhesion. Treatment with this antibody, however, only affects the migration ability of DBKO cells but not the control pLKO on a 2D random migration assay (Fig. S5 E), which is in agreement with our invasion data (Fig. 10 C-D). Integrins also provide cancer cells with increased resistance to anoikis, a programmed cell death process triggered by the lack of adhesions, through triggering FAK activation on the endosomal membrane (Alanko et al., 2015). Culturing the control and two DBKO cell lines in the low-attachment condition of agarose shows that indeed the DBKO cells form larger colonies (Fig. 10 E-F). Overall, our data provide a mechanism

bioRxiv preprint doi: https://doi.org/10.1101/2020.12.04.411645; this version posted December 4, 2020. The copyright holder for this preprint (which was not certified by peer review) is the author/funder, who has granted bioRxiv a license to display the preprint in perpetuity. It is made available under aCC-BY-NC-ND 4.0 International license.

linking the function of CYRIs in macropinocytosis to the invasive capacity of cancer cells through modulating integrin trafficking and signalling (Fig. S5 F).

bioRxiv preprint doi: https://doi.org/10.1101/2020.12.04.411645; this version posted December 4, 2020. The copyright holder for this preprint (which was not certified by peer review) is the author/funder, who has granted bioRxiv a license to display the preprint in perpetuity. It is made available under aCC-BY-NC-ND 4.0 International license.

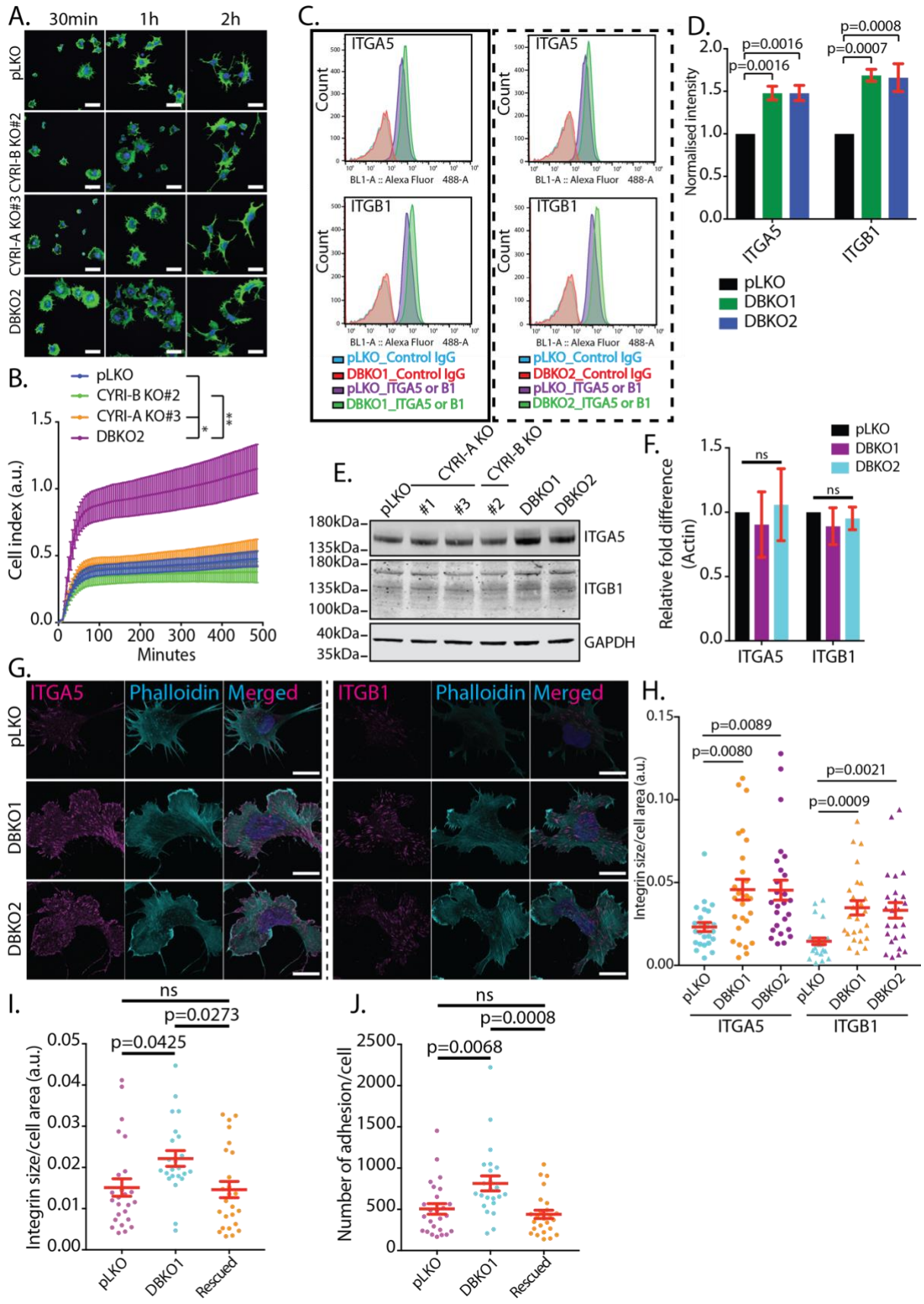

bioRxiv preprint doi: https://doi.org/10.1101/2020.12.04.411645; this version posted December 4, 2020. The copyright holder for this preprint (which was not certified by peer review) is the author/funder, who has granted bioRxiv a license to display the preprint in perpetuity. It is made available under aCC-BY-NC-ND 4.0 International license.

Fig. 8. CYRI-A and CYRI-B cooperatively regulate matrix attachment and surface expression of Integrin α5β1 in A673 cells

A-B. Representative immunofluorescence images of A-673 comparing the spreading propensity between the control pLKO and the DBKO cells on fibronectin (A). Scale bar = 40μm. The bottom graph shows the results of the Xcelligence assay comparing the cell-matrix attachment ability between the control pLKO (blue), the single knockout (green and orange) and the DBKO cells.

C-D. Flow cytometry analysis (C) and quantification (D) of the surface expression of integrin α5β1 in A-673 cells between control pLKO and the DBKO cells (DBKO1 and DBKO2).

E-F. Representative western blot of the total level of Integrin α5β1 in DBKO cells compared to control pLKO or single knockout cells (E). qPCR analysis of the gene expression of integrin α5β1 between pLKO cells and the DBKO cells (F).

G-H. Immunofluorescence images of the surface level of integrin α5β1 between control pLKO and DBKO cells (#1 and #2) (G). Scale bar = 10μm. The quantification is shown in H. Data from at least 10 cells per experiment.

I-J. Reintroduction of CYRI-A into DBKO cells is enough to reverse the effects on integrins, both in terms of area and number of integrin clusters. Data from at least 10 cells per experiment.

Data from 3 independent experiment. Mean ± SEM. Statistical analysis using ANOVA with Tukey's multiple comparisons. *$p<0.05$, **$p<0.01$.

bioRxiv preprint doi: https://doi.org/10.1101/2020.12.04.411645; this version posted December 4, 2020. The copyright holder for this preprint (which was not certified by peer review) is the author/funder, who has granted bioRxiv a license to display the preprint in perpetuity. It is made available under aCC-BY-NC-ND 4.0 International license.

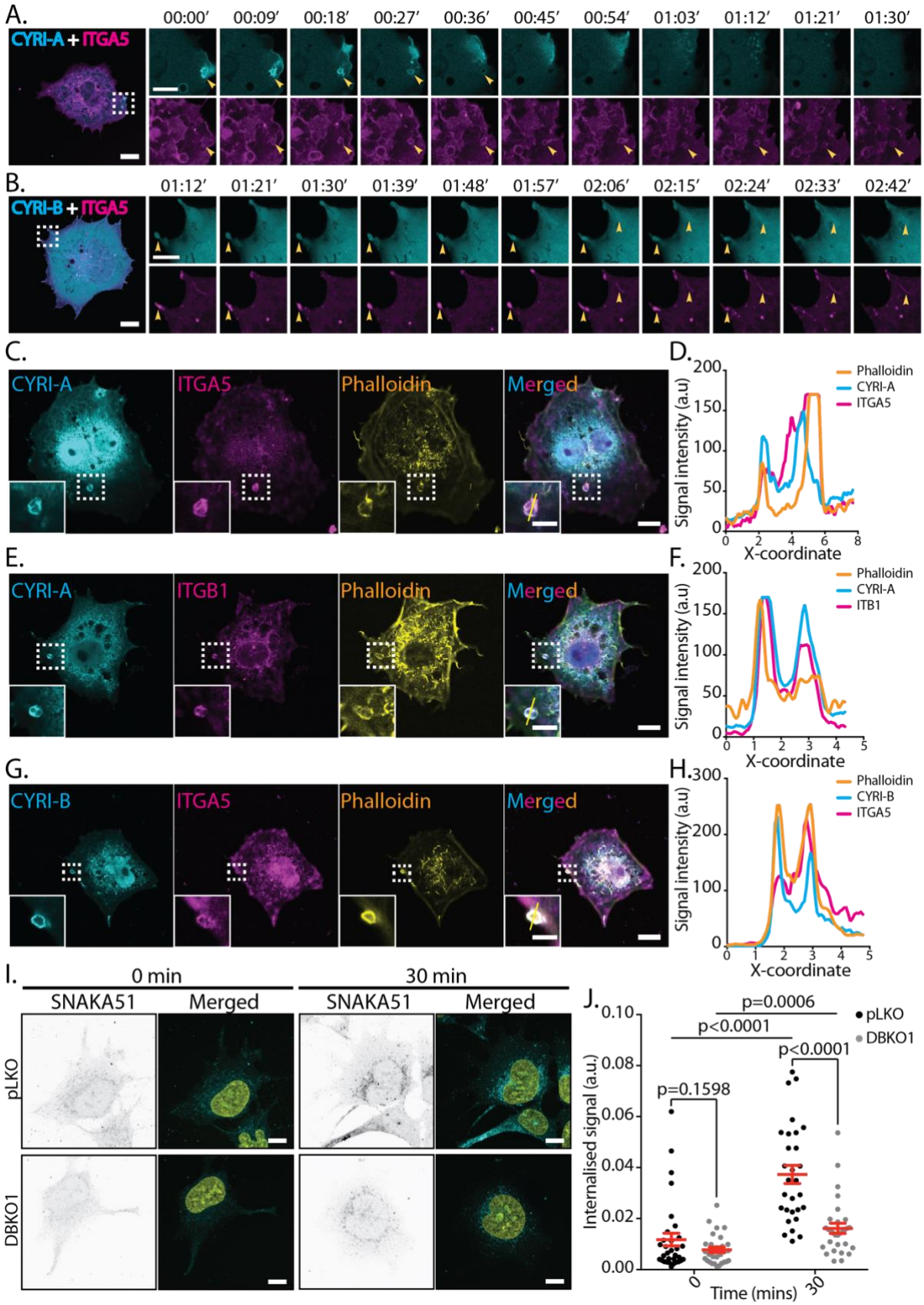

Fig. 9. (See video 19 to 20) CYRI-A and CYRI-B cooperatively regulate the internalisation of Integrin α5β1

bioRxiv preprint doi: https://doi.org/10.1101/2020.12.04.411645; this version posted December 4, 2020. The copyright holder for this preprint (which was not certified by peer review) is the author/funder, who has granted bioRxiv a license to display the preprint in perpetuity. It is made available under aCC-BY-NC-ND 4.0 International license.

A-B. Time sequence images of live COS-7 cells expressing either GFP-tagged CYRI-A or CYRI-B and mApple-tagged integrin α5. Scale bar = 10μm for full-sized image and 5μm for zooms.

C-H. Colocalisation analysis of CYRI-A or CYRI-B (cyan) with endogenous integrin α5 or β1 (magenta) and actin (orange) in COS-7 cells. Right panels (D, F, H) are intensity graph showing the colocalization of all three signals at the vesicles. Scale bar = 10μm for full-sized image and 5μm for zooms.

I-J. Internalisation assay of A-673 cells for active integrin α5 (SNAKA51, cyan) after 0- or 30-minute incubation with nuclei marked using DAPI (yellow). Left panels are representative images showing the internalised signal of active integrin α5 (SNAKA51, black signal). The right panel is the quantification of the area of the internalised signal. Data from 3 independent experiments of at least 10 cells per experiment. Statistical analysis using two-tailed unpaired t-test.

bioRxiv preprint doi: https://doi.org/10.1101/2020.12.04.411645; this version posted December 4, 2020. The copyright holder for this preprint (which was not certified by peer review) is the author/funder, who has granted bioRxiv a license to display the preprint in perpetuity. It is made available under aCC-BY-NC-ND 4.0 International license.

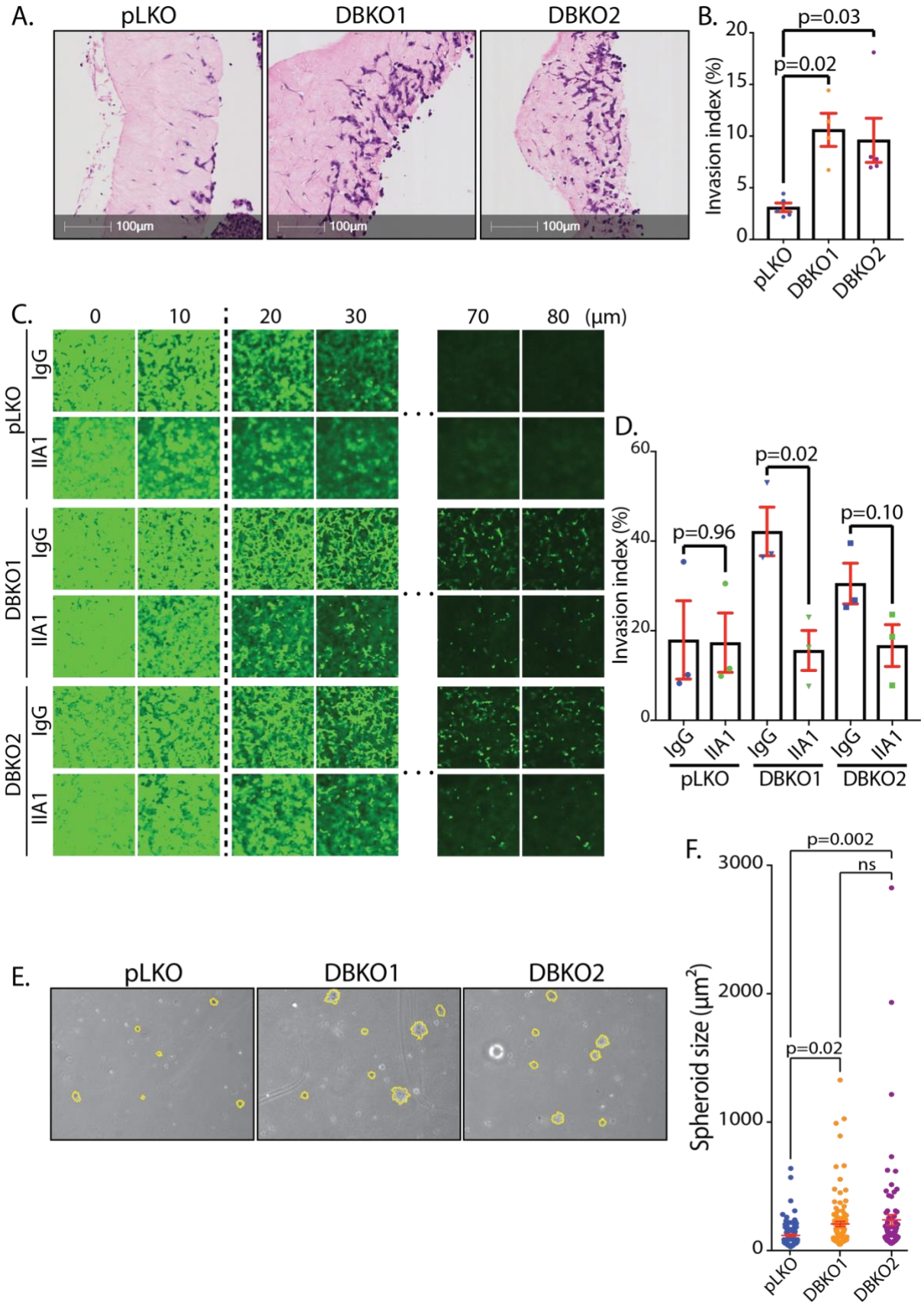

Fig. 10. CYRI proteins affect the invasion ability of cancer cells through integrins

bioRxiv preprint doi: https://doi.org/10.1101/2020.12.04.411645; this version posted December 4, 2020. The copyright holder for this preprint (which was not certified by peer review) is the author/funder, who has granted bioRxiv a license to display the preprint in perpetuity. It is made available under aCC-BY-NC-ND 4.0 International license.

A-B. Organotypic collagen plug assay of control pLKO versus DBKO of CYRI of A-673. The graph shows the quantification of the invasion index (the area invaded by cells normalised to the total area of the plug). Data are from 3 independent experiments. Mean ± SEM. Statistical analysis using ANOVA with Tukey's multiple comparisons.

C-D. Inverted invasion assay comparing the invasion capacity between the control pLKO and the DBKO of CYRI cells in the presence or absence of the integrin $\alpha5\beta1$-blocking antibody IIA1. The graph shows the quantification of the invasion index (the area covered by cells beyond 10μm into the plug). Data are from 3 independent experiments. Mean ± SEM. Statistical analysis using two-tailed unpaired t-test.

E-F. Phase-contrast images of the soft agar assay comparing the anchorage-independent growth of the control pLKO and the DBKO cells. The size of the spheroids is quantified in F.

Data are from 3 independent experiments. Mean ± SEM. Statistical analysis using ANOVA with Tukey's multiple comparisons.

Discussion

CYRI proteins show activity as negative regulators of RAC1-mediated activation of the Scar/WAVE complex, but nothing is known about their dynamic relationship with RAC1 and actin at the plasma membrane. Furthermore, the cellular functions of CYRI-A have never been specifically described. CYRI-A, encoded by the *FAM49A* gene, has previously been linked to non-syndromic oral clefts and craniofacial abnormalities (Azevedo et al., 2020; Chen et al., 2018; Leslie et al., 2016), suggesting an important role in developmental and perhaps morphogenetic processes, but a detail description of its cellular function is currently missing. Here, we model CYRI-A into the recently solved structure of CYRI-B (Kaplan et al., 2020; Yelland et al., 2020) and we conclude that CYRI-A likely adopts a similar structure to CYRI-B but may also have important differences. We show biochemically that CYRI-A interacts with active RAC1 using similar amino acid residues, but with a higher affinity than CYRI-B. CYRI-A expression can rescue the effects of CYRI-B deletion on lamellipodia and spreading, reflecting that they likely have overlapping functions. Depletion of both CYRI-A and CYRI-B together has a stronger effect on lamellipodia and cell migration than depletion of either protein independently. We

bioRxiv preprint doi: https://doi.org/10.1101/2020.12.04.411645; this version posted December 4, 2020. The copyright holder for this preprint (which was not certified by peer review) is the author/funder, who has granted bioRxiv a license to display the preprint in perpetuity. It is made available under aCC-BY-NC-ND 4.0 International license.

thus place CYRI-A as a paralog of CYRI-B, with broadly similar behaviour biochemically and in cells. However, we developed a new tool to study for the first time the dynamics of CYRI proteins and reveal a surprise dynamic role of CYRI-A in macropinocytosis, where it drives resolution of the macropinocytic cup, with implications for integrin trafficking, cell migration and invasion.

The interplay between signalling and cytoskeletal dynamics that drives macropinocytosis involves PI3K activation and PIP3 signalling leading to the activation of RAC1 (likely via recruitment of a RAC1 GEF) and thus the Scar/WAVE complex. The resulting actin assembly drives the formation of membrane ruffles and macropinosomes (Veltman et al., 2016). We observed a striking concentration of CYRI-A dynamically and transiently at macropinocytic cups, persisting until after engulfment. Using markers of the various stages of macropinocytosis, we place CYRI-A downstream of PI3K, RAC1 activation and the initiation of actin assembly at the forming macropinocytic cup. In contrast, CYRI-B appeared to be more evenly distributed at the plasma membrane and on internal tubular and vesicular structures. So, while CYRI-A and CYRI-B can compensate for each other in aspects of cell motility, they appear to be differently regulated during macropinocytosis.

Both the activation and deactivation of RAC1 are required for the completion of macropinocytosis. For example, when RAC1 activation is sustained using photoactivation, the macropinocytic cups were arrested until RAC1 activation was switched off (Fujii et al., 2013). In macrophages, RAC1 GAPs are frequently paired with GEFs (Denk-Lobnig and Martin, 2019) and are needed for the completion of phagocytosis of large particles (Schlam et al., 2015), presumably to shut down RAC1 signalling and to allow actin disassembly. However, a specific inhibitor for RAC1 at the macropinocytic cup has never been discovered. Here, we show that CYRI-A rapidly accumulates on macropinosomes harbouring activated RAC1, where it presumably disrupts RAC1 activity toward Scar/WAVE, followed by a decrease in the actin signal. Importantly, CYRI-A and actin form a feedback loop, where blocking actin dynamics using Latrunculin A or Cytochalasin D altered CYRI-A's lifetime on the vesicles, while the presence of CYRI-A decreases the lifetime of actin. Interestingly, a proteomic analysis of macropinosomes done in *Dictyostelium* also implicated CYRI (then only known as Fam49) (Journet et al., 2012), suggesting that this function is likely to be conserved. How CYRI interplays with RAC1 GEF and GAP

bioRxiv preprint doi: https://doi.org/10.1101/2020.12.04.411645; this version posted December 4, 2020. The copyright holder for this preprint (which was not certified by peer review) is the author/funder, who has granted bioRxiv a license to display the preprint in perpetuity. It is made available under aCC-BY-NC-ND 4.0 International license.

proteins is unknown, but CYRI thus far seems to be a specific locally-acting disruptor of RAC1 – Scar/WAVE signalling.

Double knockdown of CYRI-A and CYRI-B gave a robust enhancement of cell spreading and concomitant increase in surface α5β1 integrin. Integrins are internalised by multiple different routes, including macropinocytosis (Gu, et al., 2011) and the CLIC-GEEG pathway (Moreno-Layseca et al., 2020), where they can be rapidly recycled back to the surface or targeted for degradation in lysosomes (Yu et al., 2012; Zech et al., 2011). It is unclear whether certain routes of uptake such as clathrin-mediated endocytosis or macropinocytosis, might favour degradation versus recycling, but we find that by blocking CYRI's involvement in macropinocytosis, we slow down the internalisation of active integrin as detected with the SNAKA51 antibody (Fig. 9). The SNAKA51 antibody preferentially recognises active integrin α5β1 at fibrillar adhesions that are bound to fibronectin (Clark et al., 2005). Active ligand-bound α5β1 integrin is also internalised via an Arf4-Scar/WAVE-dependent manner for trafficking to lysosomes (Rainero et al., 2015). Integrin engagement and recycling are important regulators of cancer cell invasive migration (Caswell et al., 2008; Dozynkiewicz et al., 2012; Paul et al., 2015; Yu et al., 2012). Loss of CYRI-A and -B promoted cancer cell invasion, presumably due to excess active integrins on the cell surface and perhaps higher overall levels of RAC1 activation and engagement of the Scar/WAVE complex at the cell's leading edges.

We thus find that while CYRI-A has the ability to rescue the cytoskeletal defects of CYRI-B knockout cells, it shows a striking and highly dynamic localisation to macropinosomes and co-localises with integrins during their internalisation via macropinocytosis. We show that CYRI proteins regulate integrin homeostasis and loss of CYRI-A and B in a double knockout mutant leads to excessive surface integrin and an increase in invasion. Our results emphasise that activation of the Scar/WAVE complex by RAC1 not only affects cell migration and/or invasion via altering actin dynamics at the leading edge of cells, but that this pathway, regulated by CYRI proteins, is a major regulator of surface integrin levels. This could have important implications for cancers where RAC1 pathways are disrupted or enhanced, such as in melanomas where RAC1 activating mutations are considered drivers (Cannon et al., 2020).

bioRxiv preprint doi: https://doi.org/10.1101/2020.12.04.411645; this version posted December 4, 2020. The copyright holder for this preprint (which was not certified by peer review) is the author/funder, who has granted bioRxiv a license to display the preprint in perpetuity. It is made available under aCC-BY-NC-ND 4.0 International license.

Materials and methods

Cell lines generation, maintaining and growth conditions

COS-7, CHL-1 and HEK293T cells are grown in DMEM (Gibco, #21969-035) supplemented with 10% fetal bovine serum (Gibco, #10270-106) and 1X glutamine (Gibco, #25030-032) and 1X Pen/Strep (Life Technologies, #15140122). A-673 cells were a kind gift from Dr Susan Burchill, Leeds, UK and were grown in the same media but with 0.5X glutamine. Single CYRI CRISPR A-673 was generated using Lentiviral CRISPR vector (hSpCas9-2A-Puro, Addgene #62988) and selected using 1μg/ml Puromycin (Invivogen, #ant-pr-1) for 1 week. Double CYRI CRISPR A-673 was generated using the combination of the hSpCas9-2A-Puro and a modified version containing a Blasticidin resistant gene. Double knockout cells are selected by using a combination of 1μg/ml Puromycin and 6μg/ml Blasticidin (Invivogen, # ant-bl-10p) for 1 week.

For maintenance, cells are kept in the presence of all antibiotics to prevent incomplete selection. For passaging, cells are washed with PBS and 500μl of 0.25% trypsin (Gibco, #15090046) is added and incubated at 37°C for 2min. Trypsin is blocked by adding 5ml of medium containing 10%-serum and cells are split in a 1:10 ratio 2 times a week. For experimental testing, cells are grown in antibiotic-free media. Cells are grown at 37°C with 5% CO2 incubator.

sgRNA and siRNA

sgRNAs for CRISPR are designed using the Zhang lab website (https://zlab.bio/guide-design-resources) and are then purchased through ThermoFisher Scientific.

h49A-sgRNA2.1

5'-CACCGCCTGAAGGACGGCGCTGATC-3'

h49A-sgRNA2.3

5'-CACCGCTGCAGGCTTACAAAGGCGC-3'

h49B-sgRNA4.1

5'-CACCGCGAGTATGGCGTACTAGTCA-3'

siRNAs are purchased from Qiagen.

Hs_FAM49A_5 FlexiTube siRNA (#SI03150210)

Hs_FAM49A_9 FlexiTube siRNA (#SI05122656)

Hs_FAM49B_7 FlexiTube siRNA (#SI04359369)

bioRxiv preprint doi: https://doi.org/10.1101/2020.12.04.411645; this version posted December 4, 2020. The copyright holder for this preprint (which was not certified by peer review) is the author/funder, who has granted bioRxiv a license to display the preprint in perpetuity. It is made available under aCC-BY-NC-ND 4.0 International license.

AllStars Neg. Control siRNA (20nmol) (#0001027281)

For CRISPR gene deletion, lentivirus containing the CRISPR-Cas9 construct is generated using HEK293T cells. In brief, $1.5x10^6$ HEK293T cells are plated on a 10cm petri dish. Cells are transfected with 10μg of CRISPR construct containing sgRNA of the gene of interest, 7.5μg of pSPAX2 and 4μg of pVSVG packaging plasmid using standard calcium precipitation protocol (Sigma) and grown in 20% serum-containing medium for 24h. Conditioned media are filtered through a 0.45μm filter and mixed with polybrene before being added to the targeting cells. The infection process is repeated a second time before antibiotics are added during 1 week for selection.

For siRNA gene silencing, for 1 reaction, 20nmol of siRNA was mixed with 7μl of Lullaby (#LL71000, Oz Biosciences) and incubated in serum-free media in a total 200μl for 20min before adding to $3x10^5$ cells growing in 1800μl of media. The process is repeated again after 48h and cells are split if becoming too confluent. 24h after the 2nd treatment, cells are used for further experiments.

Lipofectamine plasmid transfection

For 1 reaction, 2μg of DNA plasmid is mixed with 5μl of Lipofectamine 2000 (ThermoFisher Scientifics, #11668019) in serum-free medium to a total volume of 200μl before adding to $3x10^5$ cells in a 6-well plate.

Cell fixation and Immunofluorescence

Glass coverslips are treated in concentrated HNO_3 (nitric acid) for 30min before washing with a copious amount of water. Coverslips are then coated with 1mg/ml of fibronectin (Sigma-Aldrich, #F1141) for 2h and washed with PBS. Cells are seeded on coverslips and left to settle for 4h before being fixed in 4% PFA. Cells are permeabilised with buffer containing 20mM glycine, 0.05% Tx100 in PBS for 5min before being incubated with primary and secondary antibodies. Cells are then mounted on to a glass slide using ProLong™ Diamond Antifade Mountant (#P36961, Invitrogen).

bioRxiv preprint doi: https://doi.org/10.1101/2020.12.04.411645; this version posted December 4, 2020. The copyright holder for this preprint (which was not certified by peer review) is the author/funder, who has granted bioRxiv a license to display the preprint in perpetuity. It is made available under aCC-BY-NC-ND 4.0 International license.

Image-based Integrin internalisation assay

The assay is based on the internalisation assay described in (Pietila et al., 2019) with a slight modification. In brief, A-673 cells are grown on fibronectin-coated coverslips overnight to allow the cells to fully adhere. The next day, cells are washed with ice-cold PBS and incubated with SNAKA51 antibody in ice-cold Hank's Balanced Salt Solution (HBSS) buffer that the recipe can be found here (http://cshprotocols.cshlp.org/content/2006/1/pdb.rec548.full) for 1h on ice and covered. Internalisation is induced by adding 1ml of 37°C full serum growth medium and quickly transferred to an incubator for 30min. For the control as 0min, the unbound antibody is washed with ice-cold PBS before bound antibody is stripped using acid wash (0.2M acetic acid, 0.5M NaCl, pH 2.5) for 1.5min. After 30min, antibody on the internalised cells are stripped and both conditions are fixed with 4% PFA. Cells are then subjected to our standard immunofluorescence protocol as described above. For image acquisition, a z-stack of 0.18um per slice is taken with the AiryScan Zeiss880 using the Plan-Apochromat 63x/1.4 oil DIC M27 lens. Maximum projection is generated using the 3D Project function from ImageJ. The pipeline for semi-automated quantification using auto Threshold of the image is set up using Macro recording function. The level of internalization is quantified by measuring the area of internalized signal and normalized to the size of the cell.

Macropinocytosis assay

Cells were transfected with siRNA targeting both CYRI-A and CYRI-B for 48h and 24h before seeding onto fibronectin-coated coverslips overnight. The next day, cells are washed three times with ice-cold PBS before being incubated with 0.2mg/ml dextran 70kDa (#D1822, ThermoFisher Scientific) for 15 or 30min in serum-free media at 37°C. Cells were then washed five times in ice-cold PBS and fixed for 15min using 4% paraformaldehyde before staining with DAPI for 30min. Ten random fields of view were taken and analysed using semi-automated ImageJ macro.

Western blotting

Cells are grown to 80% confluence in a 6-well plate and lysed with RIPA buffer (150mM NaCl, 10mM Tris-HCl pH7.5, 1mM EDTA, 1% Triton X-100, 0.1%SDS)

bioRxiv preprint doi: https://doi.org/10.1101/2020.12.04.411645; this version posted December 4, 2020. The copyright holder for this preprint (which was not certified by peer review) is the author/funder, who has granted bioRxiv a license to display the preprint in perpetuity. It is made available under aCC-BY-NC-ND 4.0 International license.

supplemented with protease and phosphatase inhibitor cocktails (#78438, #78427, ThermoFisher Scientific). Lysates were spun at maximum speed for 10mins before protein level is measured using Precision Red (#ADV02, Cytoskeleton, Inc.). Samples are run using precast 4-12% NuPAGE Bis-Tris Acrylamide Gels (#NP0321, ThermoFisher Scientific) and transferred to a 0.45μm nitrocellulose membrane (#10600002, GE Healthcare). Membranes are blocked in 5% BSA in TBS-T for 30min before incubated with specific primary antibodies and the corresponding secondary antibody before being analysed using the Image Studio Lite (LiCor system).

GST-Trap Pulldown

For small scale GST-tagged protein purification, BL21 competent *E. coli* is grown until OD 0.4 and induced with 200μM IPTG overnight at room temperature. Cells are pelleted and lysed using sonication in buffer containing 50mM Tris 7.5, 50mM NaCl, 5mM $MgCl_2$, 250μM DTT. The lysate is collected by ultracentrifugation at 20,000rpm for 20min. The lysate is added directly on glutathione sepharose 4B (GE Healthcare #17075601) for 2h. COS-7 cells are transfected with GFP-tagged constructs overnight and lysed the next day using lysis buffer containing 100mM NaCl, 25mM Tris-HCl pH7.5, 5mM MgCl2 supplemented with 0.5% NP-40 and protease and phosphatase inhibitors. Lysates are cleared by centrifugation and incubated with GST beads for 2h before subjected to western blotting as described.

Recombinant protein purification and surface plasmon resonance (SPR)

In brief, BL21 competent *E. coli* containing MBP-tagged or GST-tagged protein are grown to OD 0.4 and induced overnight with 200μM IPTG at room temperature. The next day, cells are concentrated and lysed using the AKTA machines in lysis buffer (20mM Tris pH 8.0, 300mM NaCl, 5mM $MgCl_2$ and 2mM beta-mercaptoethanol (BME)) supplemented with protease inhibitors. Cell lysates are cleared using ultracentrifugation at 20,000rpm for 45min. The lysate is passed through an affinity column either a MBPTrap HP (Sigma, # GE28-9187-79) or a GSTrap 4B (sigma, # GE28-4017-47) (buffer contains 20mM Tris, 150mM NaCl, 5mM $MgCl_2$ and 2mM DTT) before being eluded with either 10mM maltose or glutathione. The eluded fractions are then subjected to a size exclusion chromatography using an (HiLoad16/600

bioRxiv preprint doi: https://doi.org/10.1101/2020.12.04.411645; this version posted December 4, 2020. The copyright holder for this preprint (which was not certified by peer review) is the author/funder, who has granted bioRxiv a license to display the preprint in perpetuity. It is made available under aCC-BY-NC-ND 4.0 International license.

Superdrex 200pg). GST tags are digested overnight with thrombin and are then separated out using affinity chromatography.

For SPR: MBP-tagged proteins are immobilised on Sensor chip CM5 (GE Healthcare #BR100012) and purified untagged RAC1 Q61L is titrated at different concentrations and the response signals are recorded and fitted into a 1:1 binding model. The dissociation constant Kd is estimated from the fitted curve.

2D and 3D CDM migration assay

6-well plates are coated with 1mg/ml of fibronectin for 2h before 20,000 cells are seeded and left for 4h to settle at 37°C. Cells were imaged using the Nikon TE2000 microscope equipped with a PlanFluor 10x/0.30 objective every 15min for 20h. Individual cells were tracked overtime manually using MTrack ImageJ plug-in and the velocity is calculated using Chemotaxis tool ImageJ plug-in.

Cell-derived matrix (CDM) was generated using Telomerase Immortalised Fetal Foreskin (TIFF) cells and kept in PBS at 4°C until use (Cukierman et al., 2001). The same seeding, imaging and analysis protocol is used as for 2D migration assay.

Wound-healing assay

A 96-well plate is coated with 1mg/ml fibronectin for 2h. Cells are seeded to form a confluent monolayer (70,000 cells for A-673) and left to settle for 4h. The wound is made using the Incucyte wound maker. Cells are stained with IncuCyte Nuclight Rapid Red reagent (#4717) for total cells and IncuCyte Sytox Green reagent (#4633) for dead cells. Cells are imaged every hour for 48h using the IncuCyte system. Analysis of wound closure is done on the Zoom software (IncuCyte Biosciences, Sartorius).

Xcelligence spreading assay

XCelligence E-plate 16 (Acea #05469830001) is coated with fibronectin for 1h. Cells are trypsinised as described earlier, counted and 10,000 cells are seeded on the plate. Immediately the plate is moved to an Acea RTCA DP xCELLigence device and cell spreading is measured based on electrical impedance every 5min for 8h.

bioRxiv preprint doi: https://doi.org/10.1101/2020.12.04.411645; this version posted December 4, 2020. The copyright holder for this preprint (which was not certified by peer review) is the author/funder, who has granted bioRxiv a license to display the preprint in perpetuity. It is made available under aCC-BY-NC-ND 4.0 International license.

Airy-scan Zeiss880 super-resolution imaging

For all live imaging experiments, cells are seeded on fibronectin-coated 3.5cm dish for 4h to allow for settling. During the imaging process, cells are kept in a 37°C with 5% CO2 chamber. Latrunculin A (Sigma-Aldrich, #L5163) or Cytochalasin D (Sigma-Aldrich, #C2618) are added at 1μM. LY294002 is added at 20μM. Dextran (Texas Red™ 70,000 MW Lysine Fixable, Invitrogen, #D1864) is added at 50μg/ml. Images are taken every 9s with Plan-Apochromat 63x/1.4 oil DIC M27 lens and deconvoluted using Zeiss880 deconvolution software.

Flow cytometry analysis

$10x10^6$ cells are grown in 15cm petri dish overnight. The next day, cells are trypsinised, washed in PBS and filtered through a 40μm filter. All conditions are stained with Zombie Red reagent (#423110) before being fixed in 4% PFA for 15min. Cells are blocked in PBS supplemented with 10% serum for 30min and then incubated with the corresponding primary antibody for 15min at room temperature. If the primary antibodies are not conjugated with Alex488, cells are then incubated with the secondary antibody for 15min at room temperature before analysing using Attune NxT system. For negative control, cells are incubated with anti-human mouse IgG. For all conditions, dual colours of the far-red and 488 flow cytometry is used, hence no compensation is required. Data are imported and analysed using FlowJo software (Becton Dickinson & Company, v. 10.6.1).

Quantitative real-time PCR (qRT-PCR)

Cells are grown to 80% confluence in a 6-well plate before RNA is extracted using standard RNA extraction protocol (RNAeasy Mini Kit, Qiagen, #74104). cDNA synthesis was performed by mixing 1ug of RNA with qScript® cDNA Synthesis Kit (Quantabio, #95047-100) and the reaction condition is as following: 5min at 25°C, 30min at 42°C, 5min at 85°C using a thermocycler. qPCR is performed with the DyNAmo HS SYBR Green qPCR kit (ThermoFisher Scientific, #F410L) according to the manufacturer protocol and is done using the QuantStudio Real-Time PCR system. All primers are purchased from Qiagen website: Hs_ITGA5_1_SG QuantiTect Primer Assay (#QT00080871), Hs_ITGB1_1_SG QuantiTect Primer Assay (#QT00068124), Hs_ACT_2_SG QuantiTect Primer Assay (#QT01153551).

bioRxiv preprint doi: https://doi.org/10.1101/2020.12.04.411645; this version posted December 4, 2020. The copyright holder for this preprint (which was not certified by peer review) is the author/funder, who has granted bioRxiv a license to display the preprint in perpetuity. It is made available under aCC-BY-NC-ND 4.0 International license.

Organotypic assay

The organotypic assay is performed based on the published protocol by Dr Paul Timpson (Timpson et al., 2011). In brief, collagen is extracted from rat tail and kept in 0.5mM acetic acid buffer at 2mg/ml concentration. Collagen plugs are made by mixing TIF cells with 25ml of collagen and the pH is adjusted using NaOH to 7.2. Collagen plugs are allowed to contract for 8 days before being transferred to a 24-well plate. A-673 cells are prepared as usual without any trypsin present in the final solution and $3x10^4$ are seeded directly on top of each plug. Media are changed every 2 days for 5 days before the plugs are transferred onto a metal grid. A liquid-air interface is set up with the media acting as a chemoattractant for the invasion. Media are changed every 2 days for 14 days before the plugs were being collected and processed for H&E histology staining. Images are quantified using HALO software. Invasion index is quantified by measuring the invading area and normalised it to the size of the entire tissue section.

Inverted invasion assay

The plug was made by mixing Collagen I with Matrigel (Beckton Dickinson, #354234), fibronectin (CMF) and ice-cold PBS to the final concentration of 4, 4, 1 mg/ml respectively. 100μl of the mixture is added to each Transwell (Fisher Scientific, TKT-525-110X, C3422) with 8μm pore size and left to solidify at 37°C. $5x10^4$ A-673 cells were seeded on to the underside of the Transwell and left to adhere for 4h at 37°C. After this, the Transwell is inverted and dipped into 500μl of 10% serum-containing medium. The top chamber is filled with 100μl of serum-free medium. Inhibiting antibodies are added to the top chamber at a concentration of 5μg/ml. The cells are left to invade for 5 days before staining with 4μM Calcein AM (Invitrogen, #C1430). Z-stack images are captured every 10μm using the Olympus FV1000 confocal microscope with the UplanSApo 20x/0.74 objective. Invasion index is calculated by measuring the area of invading cells beyond 10μm in the plug and then normalised to the total area of invading cells. Area measurement is performed using an ImageJ semi-automated macro with a set threshold.

bioRxiv preprint doi: https://doi.org/10.1101/2020.12.04.411645; this version posted December 4, 2020. The copyright holder for this preprint (which was not certified by peer review) is the author/funder, who has granted bioRxiv a license to display the preprint in perpetuity. It is made available under aCC-BY-NC-ND 4.0 International license.

Low-attachment assay

Agarose is dissolved in PBS at 4% and autoclaved. Before the experiments, agarose is melted in the microwave and kept in a water bath at 65°C. To make the bottom layer, agarose solution is mixed with 10% serum media at the final concentration of 0.7% agarose. 1.5ml of this is laid to make the bottom layer. While this layer is solidifying, cells are trypsinised and made into a single-cell suspension. For the top layer, for each well, $3x10^4$ cells are mixed with the agarose and serum-containing media to the final agarose concentration of 0.35%. 1.5ml of this cell suspension is quickly dispensed on top. Finally, 2.5ml of 10% serum-containing media are pipetted on top. The cells are grown for 10 days with the media are changed every 2 days. Five random fields of cell spheroids per condition are imaged with a standard brightfield microscope. Image quantification is done manually by outlining the spheroids with the Freehand selection tool from ImageJ and the area of the spheroid are calculated. Only in-focused spheroids are measured.

Cloning and primers

Making the internal GFP or mCherry CYRI-A construct: Mouse CYRI-A cDNA is cloned into the pcDNA3.1(+) vector using standard cloning technique. HindIII and BamHI restriction sites are inserted just after codon coding for Proline 16 using the Q5-insertion mutagenesis (NEB, #E0554) according to the protocol from the manufacturer. GFP or mCherry are PCR out from pEGFP-C1 or pmCherry-N1 vector before being inserted internally of CYRI-A.

All primers are ordered from ThermoFisher Scientifics:

PCR CYRI-A

5'-TCAACGGCTAGCATGGGAAACTTGCTCAAAGTC-3'

5'-TCAACGCTCGAGTTACTGAAGCATCGCTCGAATCTG-3'

Insert restriction sites

5'-AAGCTTGCGGGATCCCACTTCTTCCTGGATTTTGAAAATG-3'

5'-GGATCCCGCAAGCTTTGGATAATTCTCAATTTCCC-3'

PCR GFP or mCherry

5'-TCAACGAAGCTTGTGAGCAAGGGCGAGGAGCTG-3'

5'-TCAACGGGATCCCTTGTACAGCTCGTCCATGCC-3'

5'-TCAACGAAGCTTGTGAGCAAGGGCGAGGAGG-3'

bioRxiv preprint doi: https://doi.org/10.1101/2020.12.04.411645; this version posted December 4, 2020. The copyright holder for this preprint (which was not certified by peer review) is the author/funder, who has granted bioRxiv a license to display the preprint in perpetuity. It is made available under aCC-BY-NC-ND 4.0 International license.

Insert Kozak sequence

5'-GCCACCATGGGAAACTTGCTCAAAGTCC-3'

5'-GCTAGCCAGCTTGGGTCT-3'

The same strategy is used to clone for P17-GFP-CYRI-B but the restriction sites are XHoI and NheI just after the codon code for Proline 17.

5'-CTCGAGGCGGCTAGCAATTTTTTCCTTGATTTTGA-3'

5'-GCTAGCCGCCTCGAGTGGCCCCTGCTCAAGGTCTG-3'

Primers for GFP-CYRI-A (1-319) and GFP-CYRI-A (29-319)

5'-TCAACGCTCGAGTGATGGGAAACTTGCTCAAAGTC-3'

5'-CATGCAGGATCCTTACTGAAGCATCGCTCGAATCTG-3'

5'-TCAACGCTCGAGTGGAAGGAGAGCGAGAGATATGG-3'

5'-CATGCAGGATCCTTATCGAATCTGTTTGGAAGTCGA-3'

Primers for the mVenus-bi-cistronic vector of CYRI-A

5'-TCAACGGCTAGCGCCACCATGGGAAACTTGCTCAAAGTC-3'

5'-TCAACGGGATCCTTACTGAAGCATCGCTCGAATCTG-3'

Primers for CYRI-A-FLAG

5'-TCAACGGGATCCGCCACCATGGGAAACTTGCTCAAAGTC-3'

5'-
TCAACGCTCGAGTTACTTGTCGTCATCGTCTTTGTAGTCCTGAAGCATCGCTCGAATCTG-
3'

Primers for MBP-CYRI-A

5'-CGTATTGGATCCATGGGAAACTTGCTCAAAGTC-3'

5'-CGTATTGAAGCTTCTACTGAAGCATCGCTCGAAT-3

GFP-PH-Grp1 is a kind gift from Dr David Bryant

Addgene plasmids

mApple-Alpha-5-Integrin (#54864)

mCherry-Clathrin LC-15 (#55019)

pcDNA3/hArf1(WT)-mCherry (#79419)

bioRxiv preprint doi: https://doi.org/10.1101/2020.12.04.411645; this version posted December 4, 2020. The copyright holder for this preprint (which was not certified by peer review) is the author/funder, who has granted bioRxiv a license to display the preprint in perpetuity. It is made available under aCC-BY-NC-ND 4.0 International license.

CAV1-mCherry (#27705)

mCherry-Rab5a-7 (#55126)

PH-Btk-GFP (#51463)

Antibodies

Anti CYRI-A antibody (Sigma-Aldrich, not in production), Anti CYRI-B antibody (Sigma-Aldrich, #HPA009076), Anti GAPDH (Millipore, #MAB374), Anti Tubulin DM1A (Sigma-Aldrich, #T6199), Anti GST (CST, #2622), Anti GFP (CST, #2955), Phalloidin 488 (Molecular Probe, #A12379), Anti-Integrin beta 1 antibody [12G10] (Abcam, #ab30394), Recombinant Anti-Integrin alpha 5 antibody [EPR7854] (Abcam, #ab150361), Anti-Integrin alpha5 (Preservative Free) Antibody, clone SNAKA51 (Millipore, #MABT201), Alexa Fluor 488 anti-human CD29 Antibody TS2/16 (BioLegend, #303015), Alexa Fluor 488 anti-mouse CD49e Antibody (BioLegend, #103810), Phospho-FAK (Tyr576/577) Antibody (CST, #3281), Anti-MMP-14 Antibody, catalytic domain, clone LEM-2/63.1 (Millipore, #MAB3329).

Statistical analysis

All statistical analyses are performed with Prism 7. All data points are pooled from independent experiments or cells and then performed the appropriate statistical test. Normality is assessed by inspecting the shape of the distribution. Parametric tests are used because they are less affected by deviation from normality distribution but are more robust than non-parametric tests (McDonald, J.H. 2014. Handbook of Biological Statistics (3rd ed.). Sparky House Publishing, Baltimore, Maryland).

Acknowledgement

We thank Dr Sue Burchill and Andrea Berry from the Leeds Institute of Cancer and Pathology, Cancer Research UK Leeds Centre for providing us with the A-673 cell line, Dr David Bryant and Dr Alvaro Roman Fernandez from the Cancer Research UK Beatson Institute and the University of Glasgow for sharing with us the PH-Grp1 construct. We thank Cancer Research UK for core funding to LMM and SI. We thank Margaret O'Prey, David Strachan and Tom Gilbey for their help with confocal microscopy, Incucyte and flow cytometry, respectively. We thank the Beatson

bioRxiv preprint doi: https://doi.org/10.1101/2020.12.04.411645; this version posted December 4, 2020. The copyright holder for this preprint (which was not certified by peer review) is the author/funder, who has granted bioRxiv a license to display the preprint in perpetuity. It is made available under aCC-BY-NC-ND 4.0 International license.

central service, the molecular service and histology service for their help with ECM plates, DNA sequencing and histology slide processing and analysis, respectively. We thank CRUK for funding the Beatson Institute (A17196 and A31287) and for funding to LMM (A24452).

bioRxiv preprint doi: https://doi.org/10.1101/2020.12.04.411645; this version posted December 4, 2020. The copyright holder for this preprint (which was not certified by peer review) is the author/funder, who has granted bioRxiv a license to display the preprint in perpetuity. It is made available under aCC-BY-NC-ND 4.0 International license.

References

Alanko, J., A. Mai, G. Jacquemet, K. Schauer, R. Kaukonen, M. Saari, B. Goud, and J. Ivaska. 2015. Integrin endosomal signalling suppresses anoikis. *Nat Cell Biol*. 17:1412-1421.

Araki, N., Y. Egami, Y. Watanabe, and T. Hatae. 2007. Phosphoinositide metabolism during membrane ruffling and macropinosome formation in EGF-stimulated A431 cells. *Exp Cell Res*. 313:1496-1507.

Araki, N., M.T. Johnson, and J.A. Swanson. 1996. A role for phosphoinositide 3-kinase in the completion of macropinocytosis and phagocytosis by macrophages. *J Cell Biol*. 135:1249-1260.

Azevedo, C.M.S., R.A. Machado, H. Martelli-Junior, S.R.A. Reis, D.C. Persuhn, R.D. Coletta, and A. Rangel. 2020. Exploring GRHL3 polymorphisms and SNP-SNP interactions in the risk of non-syndromic oral clefts in the Brazilian population. *Oral Dis*. 26:145-151.

Bianchi-Smiraglia, A., S. Paesante, and A.V. Bakin. 2013. Integrin beta5 contributes to the tumorigenic potential of breast cancer cells through the Src-FAK and MEK-ERK signaling pathways. *Oncogene*. 32:3049-3058.

Bloomfield, G., and R.R. Kay. 2016. Uses and abuses of macropinocytosis. *J Cell Sci*. 129:2697-2705.

Bohdanowicz, M., and S. Grinstein. 2013. Role of phospholipids in endocytosis, phagocytosis, and macropinocytosis. *Physiol Rev*. 93:69-106.

Buckley, C.M., and J.S. King. 2017. Drinking problems: mechanisms of macropinosome formation and maturation. *FEBS J*. 284:3778-3790.

Campa, C.C., E. Ciraolo, A. Ghigo, G. Germena, and E. Hirsch. 2015. Crossroads of PI3K and Rac pathways. *Small GTPases*. 6:71-80.

Cannon, A.C., C. Uribe-Alvarez, and J. Chernoff. 2020. RAC1 as a Therapeutic Target in Malignant Melanoma. *Trends Cancer*. 6:478-488.

Canton, J. 2018. Macropinocytosis: New Insights Into Its Underappreciated Role in Innate Immune Cell Surveillance. *Front Immunol*. 9:2286.

Carlsson, A.E. 2018. Membrane bending by actin polymerization. *Curr Opin Cell Biol*. 50:1-7.

Caswell, P.T., M. Chan, A.J. Lindsay, M.W. McCaffrey, D. Boettiger, and J.C. Norman. 2008. Rab-coupling protein coordinates recycling of alpha5beta1 integrin and EGFR1 to promote cell migration in 3D microenvironments. *J Cell Biol*. 183:143-155.

Caswell, P.T., S. Vadrevu, and J.C. Norman. 2009. Integrins: masters and slaves of endocytic transport. *Nat Rev Mol Cell Biol*. 10:843-853.

Chattaragada, M.S., C. Riganti, M. Sassoe, M. Principe, M.M. Santamorena, C. Roux, C. Curcio, A. Evangelista, P. Allavena, R. Salvia, B. Rusev, A. Scarpa, P. Cappello, and F. Novelli. 2018. FAM49B, a novel regulator of mitochondrial function and integrity that suppresses tumor metastasis. *Oncogene*. 37:697-709.

Chen, C., Q. Guo, J. Shi, X. Jiao, K. Lv, X. Liu, Y. Jiang, X. Hui, and T. Song. 2018. Genetic variants of MGMT, RHPN2, and FAM49A contributed to susceptibility of nonsyndromic orofacial clefts in a Chinese population. *J Oral Pathol Med*. 47:796-801.

Chertkova, A.O., M. Mastop, M. Postma, N. van Bommel, S. van der Niet, K.L. Batenburg, L. Joosen, T.W.J. Gadella, Y. Okada, and J. Goedhart. 2020.

bioRxiv preprint doi: https://doi.org/10.1101/2020.12.04.411645; this version posted December 4, 2020. The copyright holder for this preprint (which was not certified by peer review) is the author/funder, who has granted bioRxiv a license to display the preprint in perpetuity. It is made available under aCC-BY-NC-ND 4.0 International license.

Robust and Bright Genetically Encoded Fluorescent Markers for Highlighting Structures and Compartments in Mammalian Cells. *BioRXIV*.

Clark, K., R. Pankov, M.A. Travis, J.A. Askari, A.P. Mould, S.E. Craig, P. Newham, K.M. Yamada, and M.J. Humphries. 2005. A specific alpha5beta1-integrin conformation promotes directional integrin translocation and fibronectin matrix formation. *J Cell Sci*. 118:291-300.

Condon, N.D., J.M. Heddleston, T.L. Chew, L. Luo, P.S. McPherson, M.S. Ioannou, L. Hodgson, J.L. Stow, and A.A. Wall. 2018. Macropinosome formation by tent pole ruffling in macrophages. *J Cell Biol*. 217:3873-3885.

Cooper, J., and F.G. Giancotti. 2019. Integrin Signaling in Cancer: Mechanotransduction, Stemness, Epithelial Plasticity, and Therapeutic Resistance. *Cancer Cell*. 35:347-367.

Cukierman, E., R. Pankov, D.R. Stevens, and K.M. Yamada. 2001. Taking cell-matrix adhesions to the third dimension. *Science*. 294:1708-1712.

Denk-Lobnig, M., and A.C. Martin. 2019. Modular regulation of Rho family GTPases in development. *Small GTPases*. 10:122-129.

Dozynkiewicz, M.A., N.B. Jamieson, I. Macpherson, J. Grindlay, P.V. van den Berghe, A. von Thun, J.P. Morton, C. Gourley, P. Timpson, C. Nixon, C.J. McKay, R. Carter, D. Strachan, K. Anderson, O.J. Sansom, P.T. Caswell, and J.C. Norman. 2012. Rab25 and CLIC3 collaborate to promote integrin recycling from late endosomes/lysosomes and drive cancer progression. *Dev Cell*. 22:131-145.

Egami, Y., T. Taguchi, M. Maekawa, H. Arai, and N. Araki. 2014. Small GTPases and phosphoinositides in the regulatory mechanisms of macropinosome formation and maturation. *Front Physiol*. 5:374.

Ferreira, A.P.A., and E. Boucrot. 2018. Mechanisms of Carrier Formation during Clathrin-Independent Endocytosis. *Trends Cell Biol*. 28:188-200.

Fort, L., J.M. Batista, P.A. Thomason, H.J. Spence, J.A. Whitelaw, L. Tweedy, J. Greaves, K.J. Martin, K.I. Anderson, P. Brown, S. Lilla, M.P. Neilson, P. Tafelmeyer, S. Zanivan, S. Ismail, D.M. Bryant, N.C.O. Tomkinson, L.H. Chamberlain, G.S. Mastick, R.H. Insall, and L.M. Machesky. 2018. Fam49/CYRI interacts with Rac1 and locally suppresses protrusions. *Nat Cell Biol*. 20:1159-1171.

Fujii, M., K. Kawai, Y. Egami, and N. Araki. 2013. Dissecting the roles of Rac1 activation and deactivation in macropinocytosis using microscopic photo-manipulation. *Sci Rep*. 3:2385.

Gu, Z., E.H. Noss, V.W. Hsu, and M.B. Brenner. 2011. Integrins traffic rapidly via circular dorsal ruffles and macropinocytosis during stimulated cell migration. *J Cell Biol*. 193:61-70.

Humphreys, D., V. Singh, and V. Koronakis. 2016. Inhibition of WAVE Regulatory Complex Activation by a Bacterial Virulence Effector Counteracts Pathogen Phagocytosis. *Cell Rep*. 17:697-707.

Journet, A., G. Klein, S. Brugiere, Y. Vandenbrouck, A. Chapel, S. Kieffer, C. Bruley, C. Masselon, and L. Aubry. 2012. Investigating the macropinocytic proteome of Dictyostelium amoebae by high-resolution mass spectrometry. *Proteomics*. 12:241-245.

Kaplan, E., R. Stone, P.J. Hume, N.P. Greene, and V. Koronakis. 2020. Structure of CYRI-B (FAM49B), a key regulator of cellular actin assembly. *Acta Crystallogr D Struct Biol*. 76:1015-1024.

bioRxiv preprint doi: https://doi.org/10.1101/2020.12.04.411645; this version posted December 4, 2020. The copyright holder for this preprint (which was not certified by peer review) is the author/funder, who has granted bioRxiv a license to display the preprint in perpetuity. It is made available under aCC-BY-NC-ND 4.0 International license.

Kavran, J.M., D.E. Klein, A. Lee, M. Falasca, S.J. Isakoff, E.Y. Skolnik, and M.A. Lemmon. 1998. Specificity and promiscuity in phosphoinositide binding by pleckstrin homology domains. *J Biol Chem*. 273:30497-30508.

Lai, C.L., A. Srivastava, C. Pilling, A.R. Chase, J.J. Falke, and G.A. Voth. 2013. Molecular mechanism of membrane binding of the GRP1 PH domain. *J Mol Biol*. 425:3073-3090.

Leslie, E.J., J.C. Carlson, J.R. Shaffer, E. Feingold, G. Wehby, C.A. Laurie, D. Jain, C.C. Laurie, K.F. Doheny, T. McHenry, J. Resick, C. Sanchez, J. Jacobs, B. Emanuele, A.R. Vieira, K. Neiswanger, A.C. Lidral, L.C. Valencia-Ramirez, A.M. Lopez-Palacio, D.R. Valencia, M. Arcos-Burgos, A.E. Czeizel, L.L. Field, C.D. Padilla, E.M. Cutiongco-de la Paz, F. Deleyiannis, K. Christensen, R.G. Munger, R.T. Lie, A. Wilcox, P.A. Romitti, E.E. Castilla, J.C. Mereb, F.A. Poletta, I.M. Orioli, F.M. Carvalho, J.T. Hecht, S.H. Blanton, C.J. Buxo, A. Butali, P.A. Mossey, W.L. Adeyemo, O. James, R.O. Braimah, B.S. Aregbesola, M.A. Eshete, F. Abate, M. Koruyucu, F. Seymen, L. Ma, J.E. de Salamanca, S.M. Weinberg, L. Moreno, J.C. Murray, and M.L. Marazita. 2016. A multi-ethnic genome-wide association study identifies novel loci for non-syndromic cleft lip with or without cleft palate on 2p24.2, 17q23 and 19q13. *Hum Mol Genet*. 25:2862-2872.

Mierke, C.T., B. Frey, M. Fellner, M. Herrmann, and B. Fabry. 2011. Integrin alpha5beta1 facilitates cancer cell invasion through enhanced contractile forces. *J Cell Sci*. 124:369-383.

Millius, A., S.N. Dandekar, A.R. Houk, and O.D. Weiner. 2009. Neutrophils establish rapid and robust WAVE complex polarity in an actin-dependent fashion. *Curr Biol*. 19:253-259.

Mooren, O.L., B.J. Galletta, and J.A. Cooper. 2012. Roles for actin assembly in endocytosis. *Annu Rev Biochem*. 81:661-686.

Moreno-Layseca, P., N.Z. Jäntti, R. Godbole, C. Sommer, G. Jacquemet, H. Al-Akhrass, P. Kronqvist, R.E. Kallionpää, L. Oliveira-Ferrer, P. Cervero, S. Linder, M. Aepfelbacher, J. Rae, R.G. Parton, A. Disanza, G. Scita, S. Mayor, M. Selbach, S. Veltel, and J. Ivaska. 2020. Cargo-specific recruitment in clathrin and dynamin-independent endocytosis. *BioRXIV*.

Nam, J.M., Y. Onodera, M.J. Bissell, and C.C. Park. 2010. Breast cancer cells in three-dimensional culture display an enhanced radioresponse after coordinate targeting of integrin alpha5beta1 and fibronectin. *Cancer Res*. 70:5238-5248.

Paul, N.R., J.L. Allen, A. Chapman, M. Morlan-Mairal, E. Zindy, G. Jacquemet, L. Fernandez del Ama, N. Ferizovic, D.M. Green, J.D. Howe, E. Ehler, A. Hurlstone, and P.T. Caswell. 2015. alpha5beta1 integrin recycling promotes Arp2/3-independent cancer cell invasion via the formin FHOD3. *J Cell Biol*. 210:1013-1031.

Pietila, M., P. Sahgal, E. Peuhu, N.Z. Jantti, I. Paatero, E. Narva, H. Al-Akhrass, J. Lilja, M. Georgiadou, O.M. Andersen, A. Padzik, H. Sihto, H. Joensuu, M. Blomqvist, I. Saarinen, P.J. Bostrom, P. Taimen, and J. Ivaska. 2019. SORLA regulates endosomal trafficking and oncogenic fitness of HER2. *Nat Commun*. 10:2340.

Rainero, E., J.D. Howe, P.T. Caswell, N.B. Jamieson, K. Anderson, D.R. Critchley, L. Machesky, and J.C. Norman. 2015. Ligand-Occupied Integrin Internalization Links Nutrient Signaling to Invasive Migration. *Cell Rep*. 10:398-413.

bioRxiv preprint doi: https://doi.org/10.1101/2020.12.04.411645; this version posted December 4, 2020. The copyright holder for this preprint (which was not certified by peer review) is the author/funder, who has granted bioRxiv a license to display the preprint in perpetuity. It is made available under aCC-BY-NC-ND 4.0 International license.

Roy, A., A. Kucukural, and Y. Zhang. 2010. I-TASSER: a unified platform for automated protein structure and function prediction. *Nat Protoc*. 5:725-738.

Schlam, D., R.D. Bagshaw, S.A. Freeman, R.F. Collins, T. Pawson, G.D. Fairn, and S. Grinstein. 2015. Phosphoinositide 3-kinase enables phagocytosis of large particles by terminating actin assembly through Rac/Cdc42 GTPase-activating proteins. *Nat Commun*. 6:8623.

Schliwa, M. 1982. Action of cytochalasin D on cytoskeletal networks. *J Cell Biol*. 92:79-91.

Shang, W., Y. Jiang, M. Boettcher, K. Ding, M. Mollenauer, Z. Liu, X. Wen, C. Liu, P. Hao, S. Zhao, M.T. McManus, L. Wei, A. Weiss, and H. Wang. 2018. Genome-wide CRISPR screen identifies FAM49B as a key regulator of actin dynamics and T cell activation. *Proc Natl Acad Sci U S A*. 115:E4051-E4060.

Shi, F., and J. Sottile. 2008. Caveolin-1-dependent beta1 integrin endocytosis is a critical regulator of fibronectin turnover. *J Cell Sci*. 121:2360-2371.

Swanson, J.A., and C. Watts. 1995. Macropinocytosis. *Trends Cell Biol*. 5:424-428.

Timpson, P., E.J. McGhee, Z. Erami, M. Nobis, J.A. Quinn, M. Edward, and K.I. Anderson. 2011. Organotypic collagen I assay: a malleable platform to assess cell behaviour in a 3-dimensional context. *J Vis Exp*:e3089.

Varnai, P., T. Bondeva, P. Tamas, B. Toth, L. Buday, L. Hunyady, and T. Balla. 2005. Selective cellular effects of overexpressed pleckstrin-homology domains that recognize PtdIns(3,4,5)P3 suggest their interaction with protein binding partners. *J Cell Sci*. 118:4879-4888.

Veltman, D.M., T.D. Williams, G. Bloomfield, B.C. Chen, E. Betzig, R.H. Insall, and R.R. Kay. 2016. A plasma membrane template for macropinocytic cups. *Elife*. 5.

Yang, J., R. Yan, A. Roy, D. Xu, J. Poisson, and Y. Zhang. 2015. The I-TASSER Suite: protein structure and function prediction. *Nat Methods*. 12:7-8.

Yarmola, E.G., T. Somasundaram, T.A. Boring, I. Spector, and M.R. Bubb. 2000. Actin-latrunculin A structure and function. Differential modulation of actin-binding protein function by latrunculin A. *J Biol Chem*. 275:28120-28127.

Yelland, T., A.H. Le, S. Nikolaou, R. Insall, L. Machesky, and S. Ismail. 2020. Structural Basis of CYRI-B Direct Competition with Scar/WAVE Complex for Rac1. *Structure*.

Yoshida, S., A.D. Hoppe, N. Araki, and J.A. Swanson. 2009. Sequential signaling in plasma-membrane domains during macropinosome formation in macrophages. *J Cell Sci*. 122:3250-3261.

Yu, X., T. Zech, L. McDonald, E.G. Gonzalez, A. Li, I. Macpherson, J.P. Schwarz, H. Spence, K. Futo, P. Timpson, C. Nixon, Y. Ma, I.M. Anton, B. Visegrady, R.H. Insall, K. Oien, K. Blyth, J.C. Norman, and L.M. Machesky. 2012. N-WASP coordinates the delivery and F-actin-mediated capture of MT1-MMP at invasive pseudopods. *J Cell Biol*. 199:527-544.

Yuki, K.E., H. Marei, E. Fiskin, M.M. Eva, A.A. Gopal, J.A. Schwartzentruber, J. Majewski, M. Cellier, J.N. Mandl, S.M. Vidal, D. Malo, and I. Dikic. 2019. CYRI/FAM49B negatively regulates RAC1-driven cytoskeletal remodelling and protects against bacterial infection. *Nat Microbiol*. 4:1516-1531.

Zech, T., S.D. Calaminus, P. Caswell, H.J. Spence, M. Carnell, R.H. Insall, J. Norman, and L.M. Machesky. 2011. The Arp2/3 activator WASH regulates alpha5beta1-integrin-mediated invasive migration. *J Cell Sci*. 124:3753-3759.

bioRxiv preprint doi: https://doi.org/10.1101/2020.12.04.411645; this version posted December 4, 2020. The copyright holder for this preprint (which was not certified by peer review) is the author/funder, who has granted bioRxiv a license to display the preprint in perpetuity. It is made available under aCC-BY-NC-ND 4.0 International license.

Zhang, Y. 2008. I-TASSER server for protein 3D structure prediction. *BMC Bioinformatics*. 9:40.